

Witnessing the onset of reionisation via Lyman- α emission at redshift 13

Joris Witstok  ^{1,2,3,4*}, Peter Jakobsen  ^{3,4}, Roberto Maiolino  ^{1,2,5}, Jakob M. Helton  ⁶, Benjamin D. Johnson  ⁷, Brant E. Robertson  ⁸, Sandro Tacchella  ^{1,2}, Alex J. Cameron ⁹, Renske Smit ¹⁰, Andrew J. Bunker ⁹, Aayush Saxena ^{9,5}, Fengwu Sun ^{6,7}, Stacey Alberts ⁶, Santiago Arribas ¹¹, William M. Baker ^{1,2}, Rachana Bhatawdekar ¹², Kristan Boyett ⁹, Phillip A. Cargile ⁷, Stefano Carniani ¹³, Stéphane Charlot ¹⁴, Jacopo Chevallard ⁹, Mirko Curti ¹⁵, Emma Curtis-Lake ¹⁶, Francesco D'Eugenio ^{1,2,17}, Daniel J. Eisenstein ⁷, Kevin N. Hainline ⁶, Gareth C. Jones ^{9,1,2}, Nimisha Kumari ¹⁸, Michael V. Maseda ¹⁹, Pablo G. Pérez-González ¹¹, Pierluigi Rinaldi ⁶, Jan Scholtz ^{1,2}, Hannah Übler ²⁰, Christina C. Williams ²¹, Christopher N. A. Willmer ⁶, Chris Willott ²², and Yongda Zhu ⁶

Affiliations are listed at the end of the manuscript.

Cosmic Reionisation commenced when ultraviolet (UV) radiation produced in the first galaxies began illuminating the cold, neutral gas that filled the primordial Universe ^{1,2}. Recent James Webb Space Telescope (JWST) observations have shown that surprisingly UV-bright galaxies were in place beyond redshift $z = 14$, when the Universe was less than 300 Myr old ^{3–5}. Smooth turnovers of their UV continua have been interpreted as damping-wing absorption of Lyman- α (Ly α), the principal hydrogen transition ^{6–9}. However, spectral signatures encoding crucial properties of these sources, such as their emergent radiation field, largely remain elusive. Here we report spectroscopy from the JWST Advanced Deep Extragalactic Survey (JADES ¹⁰) of a galaxy at redshift $z = 13.0$ that reveal a singular, bright emission line unambiguously identified as Ly α , in addition to a smooth turnover. We observe an equivalent width of $\text{EW}_{\text{Ly}\alpha} > 40 \text{ \AA}$ (rest frame), previously only seen at $z < 9$ where the intervening intergalactic medium (IGM) becomes increasingly ionised ¹¹. Together with an extremely blue UV continuum, the unexpected Ly α emission indicates the galaxy is a prolific producer and leaker of ionising photons. This suggests massive, hot stars or an active galactic nucleus (AGN) have created an early reionised region to prevent complete extinction of Ly α , thus shedding new light on the nature of the earliest galaxies and the onset of Reionisation only 330 Myr after the Big Bang.

Using the Near-Infrared Camera (NIRCam ¹²) and Mid-Infrared Instrument (MIRI ¹³) on board JWST, we obtained deep imaging as part of the JADES and JADES Origins Field (JOF ¹⁴) programmes. A careful search for high-redshift galaxy candidates exploiting the 14-band NIRCam coverage ^{15,16} led to the identification of JADES-GS+53.06475-27.89024 (JADES-GS-z13-1-LA hereafter) as the most robust redshift $z \gtrsim 11.5$ photometric candidate in the JOF based on its blue colour and clear ‘dropout’ signature, confidently rejecting a brown dwarf solution. Since the discontinuity strength ($> 20\times$ in flux between the NIRCam F150W and F200W filters) further rules out a Balmer break due to an evolved stellar population at much lower redshift, the photometry strongly favours a solution at $z \approx 13$ where Ly α , the $2p \rightarrow 1s$ electronic transition of hydrogen, is shifted to 1.7 \mu m in the observed frame and any photons emitted at shorter wavelengths are completely absorbed by neutral hydrogen (H I) in the intervening IGM.

Follow-up spectroscopy of JADES-GS-z13-1-LA was obtained as part of JADES with the JWST Near-Infrared Spectrograph (NIRSpec ¹⁷), principally in PRISM mode (exposure time of 18.7 h), covering wavelengths from 0.6 \mu m up to 5.3 \mu m at low resolution ($R \approx 100$). As shown in Fig. 1, the resulting spectrum unequivocally confirms the redshift to be $z \approx 13.0$ (Methods) even if the break

is smooth rather than sharp, which indeed is expected for sources embedded in a highly neutral IGM due to Ly α damping-wing absorption ¹⁸, as has been seen directly in quasar spectra ¹⁹. Spectra of $z \gtrsim 9$ galaxies recently discovered by JWST have also hinted at the existence of IGM damping wings ^{3,7}, although many cases have been observed to far exceed pure IGM absorption, which has been ascribed to local damped Ly α (DLA) absorbing systems (column densities of $N_{\text{H}\text{I}} > 10^{20.3} \text{ cm}^{-2}$; ref. ²⁰) interpreted as pockets of dense, neutral gas within or near the galaxy ^{6,8,9,21}.

Remarkably, unlike any other $z > 10$ galaxies confirmed by JWST ^{3–6,22–24}, the PRISM spectrum additionally reveals a bright emission line detected at high signal-to-noise ratio (SNR = 6.4) and consistently across the two independent visits (Methods). Located at the blue edge of the spectral break, it is observed at $\lambda_{\text{obs}} = 1.7084 \pm 0.0014 \text{ \mu m}$ and while the continuum directly underneath is not detected, we can conservatively place a lower limit on the rest-frame EW of $> 40 \text{ \AA}$. The only viable explanation, considering the clear break and the absence of nearby foreground sources and any other lines (Methods), is to identify the line as Ly α at a redshift of $z_{\text{Ly}\alpha} = 13.05 \pm 0.01$. However, due to the resonant nature of Ly α , we note the systemic redshift is likely slightly lower.

If not arising from collisional excitation, expected to be subdominant even at interstellar medium (ISM) densities of $n \approx 10^4 \text{ cm}^{-3}$ (ref. ²⁵), this immediately implies that JADES-GS-z13-1-LA pro-

* E-mail: joris.witstok@nbi.ku.dk

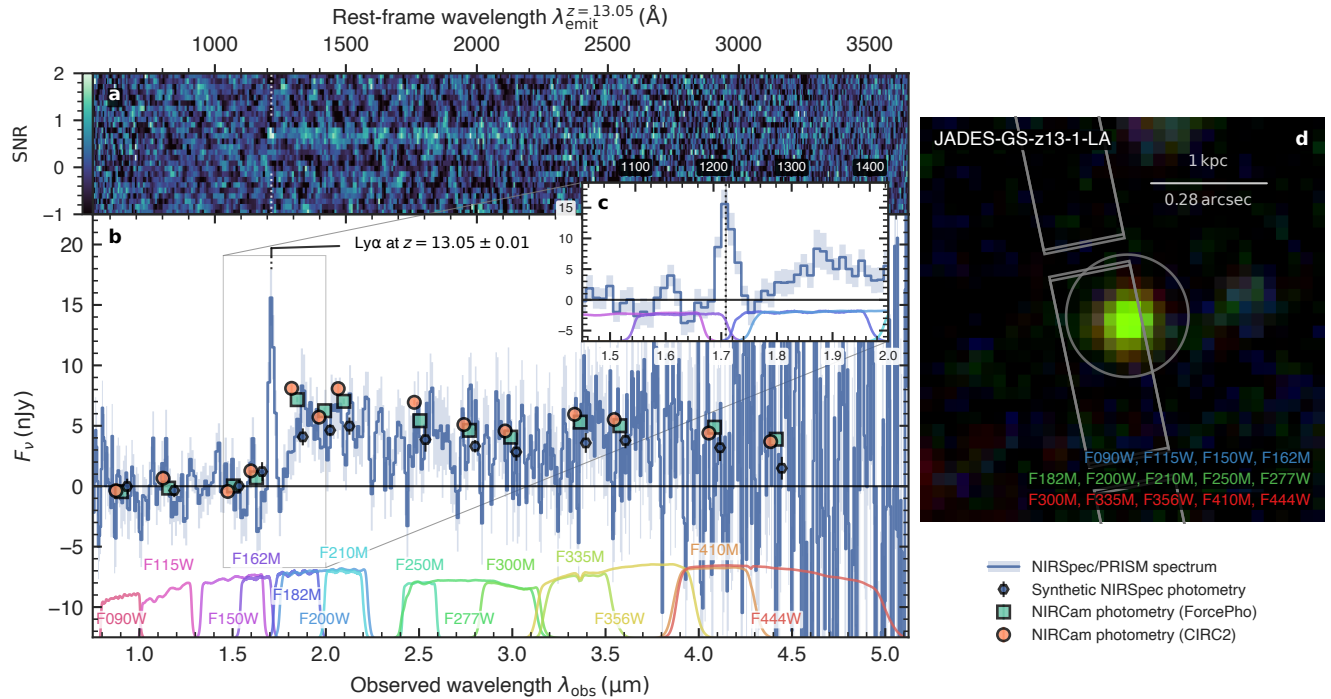


Fig. 1 | NIRCam and NIRSpec/PRISM observations of JADES-GS-z13-1-LA. **a**, Two-dimensional SNR map of the PRISM spectrum (not used for extraction of the one-dimensional spectrum; see Methods for details). **b**, One-dimensional sigma-clipped PRISM spectrum (uncorrected for additional path losses; Methods) and photometric measurements (slightly offset in wavelength for visualisation) according to the legend in the bottom right. Synthetic photometry is obtained by convolving the spectrum with the filter transmission curves shown at the bottom. Shading and error bars represent 1σ uncertainty. **c**, Zoom-in on the emission line at $1.7\text{ }\mu\text{m}$, which falls precisely in between the F162M and F182M medium-band filters. **d**, False-colour image of JADES-GS-z13-1-LA constructed by stacking NIRCam filters for each colour channel as annotated. The placement of the NIRSpec micro-shutters, nearly identical across the two visits, are shown in grey, as is the circular $0.3''$ -diameter extraction aperture for the CIRC2 photometry. A physical scale of 1 kpc ($0.28''$ at $z = 13.05$) is indicated.

duces a substantial number of ionising Lyman-continuum (LyC) photons as quantified by the production efficiency, for which we find a robust lower limit of $\xi_{\text{ion}} \gtrsim 10^{25.1}\text{ Hz erg}^{-1}$ (Methods). While already close to the canonical value required for star-forming galaxies to complete reionisation²⁶, this value increases considerably if any Ly α photons are absorbed within the galaxy or scattered out of our line of sight in the IGM. This should be a major effect at $z = 13$ as the Universe is still highly neutral^{7,19}, even if a local ionised ‘bubble’ around the galaxy facilitates the transmission of Ly α photons¹¹. Note that while photon diffusion via resonant scattering off neutral gas in the IGM is predicted to result in extended Ly α halos around galaxies before reionisation²⁷, such diffuse emission cannot explain the observed line properties. From non-detections in our medium-resolution spectra, although less sensitive than the PRISM, we do however infer the line is likely broadened spectrally (Methods).

Fitting a variety of standard stellar population synthesis (SPS) models to the observed spectral energy distribution (SED) of JADES-GS-z13-1-LA yields a young (10–20 Myr) and metal-poor (< 2% Solar) stellar population, with little to no dust obscuration (Supplementary information). However, commonly used SED fitting codes do not have the capability to model the peculiar coexistence of Ly α emission together with a smooth spectral turnover. To better understand its origin in JADES-GS-z13-1-LA, we therefore performed detailed spectral modelling where we take into account potential absorption by DLA absorbers, transmission through a neutral, mean-density IGM with a local ionised bubble, and instrumental effects such as path losses and the line spread function (LSF). For our fidu-

cial model, we opt for a power-law continuum that offers the flexibility to recreate the steep UV slope, which from the NIRCam and NIRSpec data we consistently measure to be $\beta_{\text{UV}} \lesssim -2.7$ (Methods). However, we also considered the inclusion of nebular continuum, since the two-photon (2γ) continuum in lower-redshift galaxies has been suggested^{28,29} as the potential origin of a UV turnover and Ly α emission qualitatively similar to JADES-GS-z13-1-LA. Best-fitting models with a pure power-law and 2γ continuum are shown in Fig. 2.

Regardless of the choice of continuum, our model indicates that across a range of reasonable emergent Ly α profiles, approximately 5–10% of flux may be transmitted through the IGM, implying an intrinsic Ly α luminosity of $L_{\text{Ly}\alpha} \approx 2 \times 10^{43}\text{ erg s}^{-1}$. Here, we allow for a non-zero LyC escape fraction causing a local ionised bubble with radius $R_{\text{ion}} \approx 0.2$ physical Mpc (pMpc) to form within an otherwise neutral IGM, without which the required luminosity would triple, a scenario disfavoured by the non-detection in the MIRI/F770W filter containing H β (Methods). Still, we find the models consistently require $\xi_{\text{ion}} \approx 10^{26.5}\text{ Hz erg}^{-1}$, either to create the transmission-enhancing bubble or boost the intrinsic luminosity. For any appreciable IGM transmission, the observed Ly α peak should fall substantially redwards ($\Delta v_{\text{Ly}\alpha, \text{obs}} \gtrsim 500\text{ km s}^{-1}$) of the systemic redshift^{22,30}, which we therefore infer to be $z_{\text{sys}} = 13.01^{+0.02}_{-0.01}$.

For standard stellar models, the remarkably high ξ_{ion} is untenable^{31,32} under common initial mass functions (IMFs). Since ξ_{ion} is directly sensitive to the hottest stars, its extreme value may be ascribed to an extension of the IMF to very massive stars^{33,34}. The

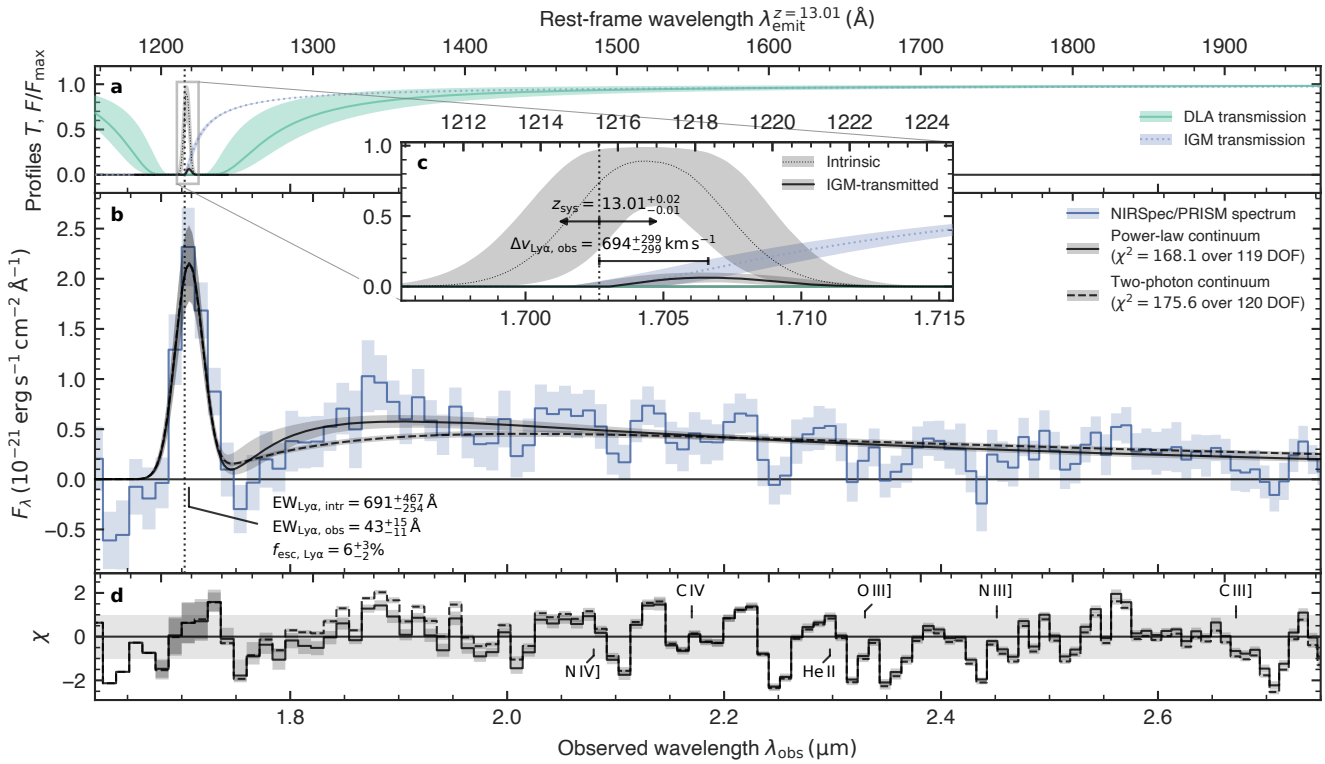


Fig. 2 | Model of NIRSpec/PRISM observations of JADES-GS-z13-1-LA. **a**, Model curves for the IGM and DLA transmission T (according to the legend on the right) and normalised Ly α line profiles (cf. panel c). **b**, A blue line shows the sigma-clipped PRISM spectrum corrected for path losses (Methods). Model spectra with a power-law continuum, and a pure 2γ continuum are shown by the black solid and dashed lines, respectively. The legend shows their χ^2 goodness-of-fit statistics compared to the degrees of freedom (DOF; Methods). The intrinsic and observed Ly α EWs (relative to an unattenuated power-law continuum), and their ratio (the escape fraction), are annotated. A similar annotation indicates upper limits on the He II line flux and EW (3σ ; Methods). **c**, Zoom-in on the intrinsic (dotted black) and IGM-transmitted (solid black) Ly α line profiles. The vertical black dotted line shows the median systemic Ly α redshift in the default model (Methods), differing from the Ly α redshift by the observed velocity offset $\Delta v_{\text{Ly}\alpha, \text{obs}}$. **d**, For the two different models, χ represents the residuals normalised by the observational uncertainty of a single wavelength bin (diagonal elements of the covariance matrix). The location of other rest-frame UV lines are indicated, though none are significantly detected (Methods). Shading represents 1σ uncertainty on all lines.

high average ionising-photon energy of a $T = 10^5$ K blackbody moreover yields a $2\times$ higher ratio of Ly α to LyC photons than standard case-B recombination²⁵, thereby bringing the true ξ_{ion} more closely in agreement with the theoretical stellar maximum³⁵. One particularly intriguing class of objects predicted to radiate up to 40% of their bolometric luminosity as Ly α are entirely metal-free Population III (Pop III) stars^{36–38} thought to reach significantly higher masses and effective temperatures than subsequent metal-enriched stellar populations. However, the absolute UV magnitude of JADES-GS-z13-1-LA, $M_{\text{UV}} \approx -18.7$ mag, would require a stellar mass of $M_* \approx 10^6 M_\odot$ as a pure Pop III system, somewhat higher than typical predictions³⁹. Furthermore, the absence of strong He II $\lambda 1640$ Å emission (Methods) may argue against the Pop III scenario⁴⁰, though its strength rapidly evolves a few Myr after a star formation burst^{37,38}.

The presence of extraordinarily hot stars ($T_{\text{eff}} > 10^5$ K) required to explain such high ξ_{ion} could naturally lead relatively low-density gas ($n \lesssim 10^4 \text{ cm}^{-3}$) to emit a prominent nebular continuum with a UV turnover^{29,41}. However, we find that compared to the pure 2γ continuum, which only becomes further reddened by free-bound continuum emission at higher densities, the current data are better reproduced by a steep power law (Fig. 2). A scenario where Ly α emission is produced together with 2γ continuum as cooling radiation via collisional excitation in the dense core of a collapsing cloud⁴²

is therefore also disfavoured. The extremely blue UV continuum ($\beta_{\text{UV}} \lesssim -2.7$) consistently leads our models to prefer near-unity LyC escape fraction to reproduce the blue SED of JADES-GS-z13-1-LA, even with an IMF extending to $300 M_\odot$ (Methods). Moreover, recent stellar models show⁴³ the effective temperatures of very massive stars stagnate beyond $100 M_\odot$, suggesting a high LyC escape fraction remains necessary. While this would corroborate the suggestion that JADES-GS-z13-1-LA is located inside an ionised bubble and could suppress He II, it still leaves the UV turnover to be explained.

Instead, the spectrum of JADES-GS-z13-1-LA therefore appears to necessitate significant DLA absorption ($N_{\text{H}_1} \approx 10^{22.8} \text{ cm}^{-2}$ for the power-law continuum), as seen in several $z > 10$ galaxies^{6,8,9,21}. If the DLA absorber were co-located with the galaxy, a specific geometry is required to simultaneously accommodate the escape of Ly α and potentially LyC. As illustrated in Fig. 3, an inhomogeneous ISM or an edge-on disc and associated ionisation cone may cause DLA absorption in compact continuum sources which is circumvented by Ly α emission⁴⁴. Especially in the absence of dust, Ly α emission could escape through resonant scattering while also becoming broadened in velocity space, consistent with observations. Empirically, Ly α emission superimposed on DLA absorption has not only been reported for nearby UV-bright star-forming galaxies where

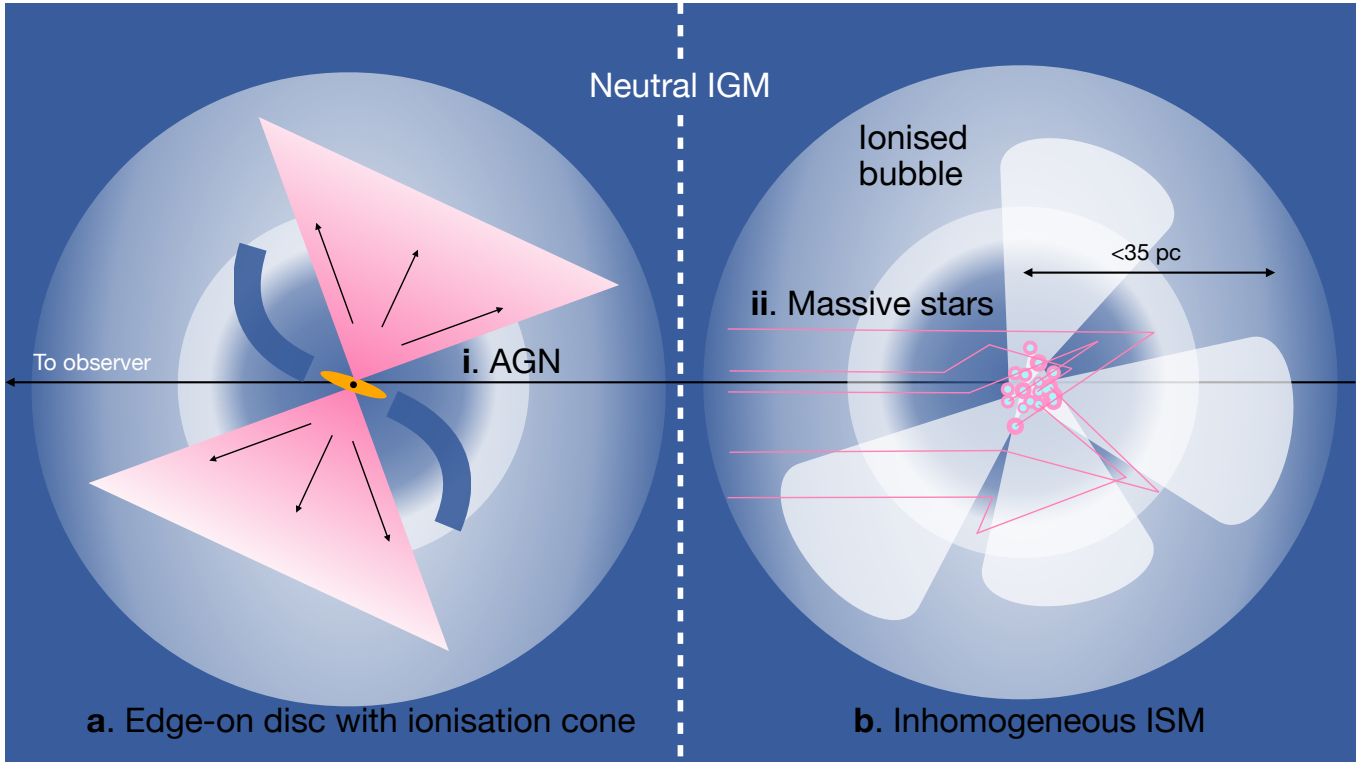


Fig. 3 | Schematic of production, escape, and absorption of Ly α in JADES-GS-z13-1-LA. Ly α emission is indicated in pink, whereas dark blue shows H α gas. We identify two potential explanations each for the source of emission (i and ii) and modes of Ly α modulation (a and b). An extended disc of neutral gas seen in edge-on orientation (a) may cause DLA absorption of the continuum source, while an ionisation cone perpendicular to the disc plane allows Ly α photons to escape. Under this escape mechanism, the source of the Ly α emission may be interchanged from an AGN (i) to a nuclear starburst (ii). Alternatively, if neutral gas in the ISM is inhomogeneously distributed (b), resonant scattering could allow Ly α to diffuse outwards while the central source remains obscured by H α gas, as seen in local, compact star-forming galaxies (see text for details).

it has been interpreted as a sign of ISM inhomogeneity⁴⁵, but also in the case of AGN⁴⁶.

Indeed, an accreting supermassive black hole (SMBH) may offer a comprehensive alternative explanation for the observed properties of JADES-GS-z13-1-LA. Effectively unresolved by NIRCam, its half-light radius of $\lesssim 35$ pc (Methods) is smaller than most $z > 10$ galaxies^{3,5,22,23}. AGN have been observed⁴⁷ to reach UV slopes significantly steeper than the standard thin-disc model⁴⁸ with $\beta_{\text{UV}} = 7/3 \approx -2.33$, as expected for a truncated accretion disc. They are also found⁴⁹ to have high LyC escape fractions, and the broad Ly α line could be linked to AGN-driven outflows or a broad line region. Constraints on the currently undetected He II and other UV lines (Methods) are consistent with model predictions for metal-poor AGN⁴⁰, altogether rendering JADES-GS-z13-1-LA a viable candidate.

Whether the Ly α emission of JADES-GS-z13-1-LA originates in stars or a SMBH, it reveals the rather extreme character of one of the earliest galaxies known, despite having been found in a modest survey area¹⁶ probing a comoving volume of 50 000 Mpc³ between $z = 11$ and $z = 15$. At just 330 Myr after the Big Bang, the likely presence of a reionised region around this relatively UV-faint source readily constrains the timeline of cosmic reionisation, favouring an early and gradual process driven (initially) by low-mass galaxies⁵⁰. Furthermore, it provides tangible evidence for the Wouthuysen-Field coupling of the spin temperature of neutral hydrogen to that of the gas via the emission of Ly α photons, the global evolution of which

is anticipated to be uncovered soon by H α 21 cm experiments⁵¹ to provide a complementary view of Cosmic Dawn.

References

1. Dayal P., Ferrara A., 2018. Early galaxy formation and its large-scale effects, *Phys. Rep.*, **780**, 1
2. Robertson B. E., 2022. Galaxy Formation and Reionization: Key Unknowns and Expected Breakthroughs by the James Webb Space Telescope, *ARA&A*, **60**, 121
3. Curtis-Lake E., et al., 2023. Spectroscopic confirmation of four metal-poor galaxies at $z = 10.3\text{--}13.2$, *Nature Astronomy*, **7**, 622
4. Arrabal Haro P., et al., 2023. Confirmation and refutation of very luminous galaxies in the early Universe, *Nature*, **622**, 707
5. Carniani S., et al., 2024. Spectroscopic confirmation of two luminous galaxies at a redshift of 14, *Nature*, **633**, 318
6. D'Eugenio F., et al., 2024. JADES: Carbon enrichment 350 Myr after the Big Bang, *A&A*, **689**, A152
7. Hsiao T. Y.-Y., et al., 2024. JWST NIRSpec Spectroscopy of the Triply Lensed $z = 10.17$ Galaxy MACS0647-JD, *ApJ*, **973**, 8
8. Heintz K. E., et al., 2024. Strong damped Lyman- α absorption in young star-forming galaxies at redshifts 9 to 11, *Science*, **384**, 890
9. Hainline K. N., et al., 2024. Searching for Emission Lines at $z > 11$: The Role of Damped Ly α and Hints About the Escape of Ionizing Photons, *ApJ*, **976**, 160

10. Eisenstein D. J., et al., 2023. Overview of the JWST Advanced Deep Extragalactic Survey (JADES), p. [arXiv:2306.02465](https://arxiv.org/abs/2306.02465)
11. Witstok J., et al., 2025. JADES: primaeval Lyman α emitting galaxies reveal early sites of reionization out to redshift $z \sim 9$, *MNRAS*, **536**, 27
12. Rieke M. J., et al., 2023. Performance of NIRCam on JWST in Flight, *PASP*, **135**, 028001
13. Rieke G. H., et al., 2015. The Mid-Infrared Instrument for the James Webb Space Telescope, I: Introduction, *PASP*, **127**, 584
14. Eisenstein D. J., et al., 2023. The JADES Origins Field: A New JWST Deep Field in the JADES Second NIRCam Data Release, p. [arXiv:2310.12340](https://arxiv.org/abs/2310.12340)
15. Hainline K. N., et al., 2024. The Cosmos in Its Infancy: JADES Galaxy Candidates at $z > 8$ in GOODS-S and GOODS-N, *ApJ*, **964**, 71
16. Robertson B., et al., 2024. Earliest Galaxies in the JADES Origins Field: Luminosity Function and Cosmic Star Formation Rate Density 300 Myr after the Big Bang, *ApJ*, **970**, 31
17. Jakobsen P., et al., 2022. The Near-Infrared Spectrograph (NIRSpec) on the James Webb Space Telescope. I. Overview of the instrument and its capabilities, *A&A*, **661**, A80
18. Miralda-Escudé J., 1998. Reionization of the Intergalactic Medium and the Damping Wing of the Gunn-Peterson Trough, *ApJ*, **501**, 15
19. Bañados E., et al., 2018. An 800-million-solar-mass black hole in a significantly neutral Universe at a redshift of 7.5, *Nature*, **553**, 473
20. Wolfe A. M., Gawiser E., Prochaska J. X., 2005. Damped Ly α Systems, *ARA&A*, **43**, 861
21. Carniani S., et al., 2024. The eventful life of a luminous galaxy at $z = 14$: metal enrichment, feedback, and low gas fraction?, p. [arXiv:2409.20533](https://arxiv.org/abs/2409.20533)
22. Bunker A. J., et al., 2023. JADES NIRSpec Spectroscopy of GN-z11: Lyman- α emission and possible enhanced nitrogen abundance in a $z = 10.60$ luminous galaxy, *A&A*, **677**, A88
23. Wang B., et al., 2023. UNCOVER: Illuminating the Early Universe-JWST/NIRSpec Confirmation of $z > 12$ Galaxies, *ApJ*, **957**, L34
24. Harikane Y., et al., 2024. Pure Spectroscopic Constraints on UV Luminosity Functions and Cosmic Star Formation History from 25 Galaxies at $z_{spec} = 8.61-13.20$ Confirmed with JWST/NIRSpec, *ApJ*, **960**, 56
25. Raiter A., Schaerer D., Fosbury R. A. E., 2010. Predicted UV properties of very metal-poor starburst galaxies, *A&A*, **523**, A64
26. Robertson B. E., Ellis R. S., Furlanetto S. R., Dunlop J. S., 2015. Cosmic Reionization and Early Star-forming Galaxies: A Joint Analysis of New Constraints from Planck and the Hubble Space Telescope, *ApJ*, **802**, L19
27. Loeb A., Rybicki G. B., 1999. Scattered Ly α Radiation around Sources before Cosmological Reionization, *ApJ*, **524**, 527
28. Hall P. B., et al., 2004. A Ly α -only Active Galactic Nucleus from the Sloan Digital Sky Survey, *AJ*, **127**, 3146
29. Cameron A. J., et al., 2024. Nebular dominated galaxies: insights into the stellar initial mass function at high redshift, *MNRAS*, **534**, 523
30. Scholtz J., et al., 2024. GN-z11: The environment of an active galactic nucleus at $z = 10.603$. New insights into the most distant Ly α detection, *A&A*, **687**, A283
31. Topping M. W., et al., 2022. Searching for Extremely Blue UV Continuum Slopes at $z = 7-11$ in JWST/NIRCam Imaging: Implications for Stellar Metallicity and Ionizing Photon Escape in Early Galaxies, *ApJ*, **941**, 153
32. Eldridge J. J., Stanway E. R., 2022. New Insights into the Evolution of Massive Stars and Their Effects on Our Understanding of Early Galaxies, *ARA&A*, **60**, 455
33. Maseda M. V., et al., 2020. Elevated ionizing photon production efficiency in faint high-equivalent-width Lyman- α emitters, *MNRAS*, **493**, 5120
34. Vanzella E., et al., 2023. An extremely metal-poor star complex in the reionization era: Approaching Population III stars with JWST, *A&A*, **678**, A173
35. Schaerer D., Guibert J., Marques-Chaves R., Martins F., 2024. Observable and ionizing properties of star-forming galaxies with very massive stars and different IMFs, p. [arXiv:2407.12122](https://arxiv.org/abs/2407.12122)
36. Schaerer D., 2002. On the properties of massive Population III stars and metal-free stellar populations, *A&A*, **382**, 28
37. Katz H., Kimm T., Ellis R. S., Devriendt J., Slyz A., 2023. The challenges of identifying Population III stars in the early Universe, *MNRAS*, **524**, 351
38. Trussler J. A. A., et al., 2023. On the observability and identification of Population III galaxies with JWST, *MNRAS*, **525**, 5328
39. Bromm V., Yoshida N., 2011. The First Galaxies, *ARA&A*, **49**, 373
40. Nakajima K., Maiolino R., 2022. Diagnostics for PopIII galaxies and direct collapse black holes in the early universe, *MNRAS*, **513**, 5134
41. Katz H., et al., 2024. 21 Balmer Jump Street: The Nebular Continuum at High Redshift and Implications for the Bright Galaxy Problem, UV Continuum Slopes, and Early Stellar Populations, p. [arXiv:2408.03189](https://arxiv.org/abs/2408.03189)
42. Dijkstra M., 2009. Continuum Emission by Cooling Clouds, *ApJ*, **690**, 82
43. Martins F., Palacios A., 2022. Spectroscopic evolution of very massive stars at $Z = 1/2.5 Z_{\odot}$, *A&A*, **659**, A163
44. Tacchella S., et al., 2024. Resolving the nature and putative nebular emission of GS9422: an obscured AGN without exotic stars, p. [arXiv:2404.02194](https://arxiv.org/abs/2404.02194)
45. Hu W., et al., 2023. CLASSY VII Ly α Profiles: The Structure and Kinematics of Neutral Gas and Implications for LyC Escape in Reionization-era Analogs, *ApJ*, **956**, 39
46. Wu S., et al., 2024. Discovery of a damped Ly α absorber in the circumnuclear zone of the FeLoBAL quasar SDSS J083942.11+380526.3, *MNRAS*, **532**, 4703
47. Tang J.-J., et al., 2019. Rapid black hole growth at the dawn of the Universe: a super-Eddington quasar at $z = 6.6$, *MNRAS*, **484**, 2575
48. Shakura N. I., Sunyaev R. A., 1973. Black holes in binary systems. Observational appearance., *A&A*, **24**, 337
49. Grazian A., et al., 2018. The contribution of faint AGNs to the ionizing background at $z > 4$, *A&A*, **613**, A44
50. Qin Y., Wyithe J. S. B., 2025. Reionization morphology and intrinsic velocity offsets allow transmission of Lyman- α emission from JADES-GS-z13-1-LA., *MNRAS*,
51. de Lera Acedo E., et al., 2022. The REACH radiometer for detecting the 21-cm hydrogen signal from redshift $z \approx 7.5-28$, *Nature Astronomy*, **6**, 984

Methods

Cosmology and conventions

A flat Λ CDM cosmology is adopted throughout based on the latest results of the Planck collaboration⁵², with $H_0 = 67.4 \text{ km s}^{-1} \text{ Mpc}^{-1}$, $\Omega_m = 0.315$, $\Omega_b = 0.0492$. The cosmic hydrogen fraction is fixed to $f_H = 0.76$. At $z = 13$, the Hubble flow is $H(z = 13) \approx 1990 \text{ km s}^{-1} \text{ Mpc}^{-1}$, and on-sky separations of $1''$ and $1'$ correspond to 3.53 physical kpc (pkpc) and 0.212 pMpc, respectively. We quote magnitudes in the AB system⁵³, emission-line wavelengths in vacuum, and EWs in the rest frame unless explicitly mentioned otherwise.

NIRCam observations and target selection

In the following sections, we describe the main JWST and auxiliary Hubble Space Telescope (HST) observations underlying this work. We refer to Robertson et al.¹⁶ and Helton et al.⁵⁴ for details on the NIRCam and MIRI imaging, respectively, while Carniani et al.⁵ provide a detailed description of the NIRSpec spectroscopy. Further details on the JADES survey strategy and data reduction are discussed in the survey overview paper¹⁰ and the data release papers^{55–57}.

The NIRCam¹², MIRI¹³ and NIRSpec^{17, 58} measurements presented in this work are associated with JWST guaranteed time observations (GTO) programme IDs (PIDs) 1180 (PI: Eisenstein), 1210, 1286, and 1287 (PI: Luetzendorf), further complemented with the JOF programme¹⁴ (PID 3215, PIs: Eisenstein & Maiolino). In addition, since the JOF itself is located within the Great Observatories Origins Deep Survey-South (GOODS-S⁵⁹) extragalactic legacy field, HST Legacy Fields imaging⁶⁰ is publicly available, covering $0.4 \mu\text{m}$ to $1.8 \mu\text{m}$ between the Advanced Camera for Surveys (ACS) and Wide Field Camera 3 (WFC3).

Additional MIRI imaging in the F770W filter was obtained⁵⁴ as coordinated parallel observations to JADES NIRCam observations (PID 1180). Several high-redshift targets, selected by Hainline et al.¹⁵ and Robertson et al.¹⁶ based on the NIRCam images in the JOF, including JADES-GS-z13-1-LA^{*}, were followed up using the NIRSpec micro-shutter array (MSA⁶¹) as part of PID 1287, scheduled between 10 and 12 January 2024.

NIRSpec observations and data reduction

The NIRSpec observations spanned three consecutive visits, however during visit 2 the lock on the guide star was lost, preventing it from being carried out nominally. While different MSA configurations were adopted across visits, JADES-GS-z13-1-LA was observed in both visits 1 and 3 in the PRISM/CLEAR grating-filter combination (simply ‘PRISM’ hereafter) with resolving power of $30 \lesssim R \lesssim 300$ between wavelengths of $0.6 \mu\text{m}$ and $5.3 \mu\text{m}$, as well as in the medium-resolution grating-filter combinations G140M/F070LP, G235M/F170LP, and G395M/F290LP (‘R1000 gratings’), each with resolving power $R \approx 1000$. A sequence of exposures following three nod positions was repeated four times for each visit in PRISM mode, and once for each of the R1000 gratings. Each nod sequence had an exposure time of 8403.2 s , consisting of six integrations made up

of 19 groups in NRSIRS2 readout mode⁶². Altogether, JADES-GS-z13-1-LA was observed for 67225.6 s by the NIRSpec/PRISM and 16806.4 s in each of the R1000 gratings.

We employed version 3.1 of the data reduction pipeline developed by the ESA NIRSpec Science Operations Team⁶¹ and the NIRSpec GTO team (simply ‘pipeline’ hereafter), which produces flux-calibrated spectra largely following the algorithms adopted in the Space Telescope Science Institute (STScI) pipeline[†]. We refer to previous works^{3, 5, 56, 57} for detailed descriptions of the NIRSpec data reduction pipeline, an overview of which is given in Ferruit et al.⁶¹. In brief, three adjacent micro-shutters were opened to obtain background-subtracted spectra of individual sources, where the subtraction follows a three-point nodding scheme discussed above. Initial path-loss corrections were calculated under the assumption of a point-source light profile placed at the same intra-shutter location of the source. The PRISM spectra adopt an irregular wavelength grid with sampling such that the wavelength-dependent LSF¹⁷ always spans a fixed number of wavelength bins. Our fiducial (‘sigma-clipped’) spectrum combines all available sub-exposures in the three nodding positions, for which one-dimensional spectra are extracted over the central three spatial pixels (corresponding to $0.3''$), via a custom sigma-clipping algorithm (see Supplementary information for details).

Photometric measurements

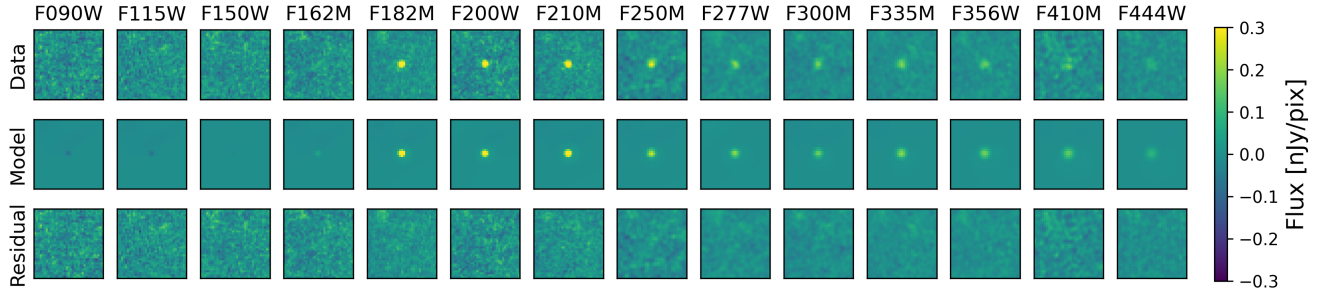
We obtained photometric measurements of JADES-GS-z13-1-LA via two methods. Our fiducial photometry is determined using FORCEPHO (Johnson et al. in prep.) on all 14 available NIRCam filters (see also Robertson et al.¹⁶), while the MIRI/F770W follows a customised procedure following Helton et al. (in prep.), both discussed in more detail below. An alternative approach to FORCEPHO is to measure fluxes in circular apertures with a diameter of $0.3''$ (‘CIRC2’). These results are summarised in Extended Data Table 1. We include CIRC2 photometry in the available HST bands, which, together with NIRCam filters up to and including F150W, are statistically fully consistent with non-detections ($\chi^2 = 11.6$ over 10 filters, i.e. $p = 0.31$).

Given the full-width half maximum (FWHM) of the MIRI/F770W point spread function (PSF) is significantly larger than those of NIRCam⁵⁴, we considered the F444W – F770W colour of JADES-GS-z13-1-LA after convolving the F444W mosaic with the F770W PSF and rebinning to the F770W pixel size. We measured this colour assuming a circular aperture with $0.7''$ diameter (‘CIRC5’), which roughly corresponds to the 65% encircled energy of F770W, prior to applying aperture corrections. The reported MIRI/F770W flux is then inferred from the difference between the total CIRC5 NIRCam/F444W flux and the F444W – F770W colour. By adopting this approach, we are taking advantage of the higher spatial resolution afforded by NIRCam compared to MIRI. However, this measurement does not yield a significant detection ($F_\nu = 1.60 \pm 2.23 \text{ nJy}$). Neglecting contributions from the [O III] $\lambda 4960, 5008 \text{ \AA}$ lines and underlying continuum, the MIRI non-detection would be consistent with an H β flux of $F_{\text{H}\beta} \lesssim 6.7 \times 10^{-19} \text{ erg s}^{-1} \text{ cm}^{-2}$ (3σ), translating to an intrinsic Ly α flux of $F_{\text{Ly}\alpha} \lesssim 1.6 \times 10^{-17} \text{ erg s}^{-1} \text{ cm}^{-2}$ (case-B recombination; e.g. ref.¹¹).

To explore the morphology of JADES-GS-z13-1-LA, we first fitted Sérsic⁶³ profiles separately to the various available NIRCam filters (using the mosaic images) employing the PYSERSC code⁶⁴. We do

* Located at right ascension of $+53.06475 \text{ deg}$ and declination of -27.89024 deg .

† <https://jwst-docs.stsci.edu/jwst-science-calibration-pipeline>



Extended Data Fig. 1 | forcepho modelling of JADES-GS-z13-1-LA. The top row shows $\sim 1'' \times 1''$ cutouts of the observed data (scaled according to the colourbar shown on the right) around JADES-GS-z13-1-LA in each of the 14 available NIRCam filters, as annotated at the top of each column. The PSF-convolved forcepho model (see Photometric measurements) is shown in the middle row. The bottom row shows residuals between data and model are consistent with pure noise, indicating the model provides a good fit to the data. Note that while the forcepho fits are performed on > 400 separate exposures, they are mosaiced together here to visualise the data and residuals.

Extended Data Table 1 | Photometry and UV-continuum properties of JADES-GS-z13-1-LA.

Quantity	Instrument	Filter (set)	ForcePho	CIRC2	Synthetic (NIRSpec)
HST/ACS	HST/ACS	F435W	...	2.37 ± 3.81	...
		F606W	...	-0.80 ± 3.02	...
		F775W	...	-3.00 ± 4.34	...
		F814W	...	6.11 ± 3.79	...
		F850LP	...	-2.25 ± 7.35	...
HST/WFC3	HST/WFC3	F125W	...	-34.6 ± 15.9	...
		F160W	...	-12.1 ± 22.0	...
Flux density F_ν (nJy)	JWST/NIRCam	F090W	-0.448 ± 0.190	-0.372 ± 0.609	-0.023 ± 0.641
		F115W	-0.157 ± 0.163	0.664 ± 0.496	-0.354 ± 0.551
		F150W	0.023 ± 0.183	-0.430 ± 0.480	0.013 ± 0.515
		F162M	0.696 ± 0.211	1.270 ± 0.566	1.212 ± 0.780
		F182M	7.164 ± 0.201	8.097 ± 0.331	4.082 ± 0.701
		F200W	6.248 ± 0.267	5.718 ± 0.488	4.632 ± 0.496
		F210M	7.025 ± 0.245	8.077 ± 0.416	4.973 ± 0.712
		F250M	5.421 ± 0.397	6.941 ± 0.211	3.857 ± 0.998
		F277W	4.624 ± 0.259	5.101 ± 0.183	3.309 ± 0.511
		F300M	4.061 ± 0.231	4.569 ± 0.166	2.835 ± 0.729
		F335M	5.304 ± 0.310	5.951 ± 0.173	3.582 ± 0.821
		F356W	5.008 ± 0.296	5.514 ± 0.199	3.787 ± 0.644
		F410M	4.883 ± 0.513	4.400 ± 0.320	3.19 ± 1.10
		F444W	3.890 ± 0.433	3.692 ± 0.273	1.488 ± 0.942
	JWST/MIRI	F770W		1.60 ± 2.23	
UV magnitude M_{UV} (mag)	JWST/MIRI	F210M through F444W	$-18.492^{+0.039}_{-0.038}$	$-18.601^{+0.036}_{-0.035}$	$-18.03^{+0.15}_{-0.13}$
Bolometric luminosity L_{bol} ($10^{10} L_\odot$)		F210M through F444W	$9.0^{+1.6}_{-1.4}$	$9.6^{+1.4}_{-1.2}$	$7.8^{+6.6}_{-3.5}$
UV slope (up to 5 μm) β_{UV}		F210M through F444W	$-2.75^{+0.10}_{-0.10}$	$-2.719^{+0.082}_{-0.082}$	$-2.88^{+0.36}_{-0.37}$
UV slope (up to 3.5 μm) $\hat{\beta}_{\text{UV}}$		F210M through F335M	$-3.10^{+0.14}_{-0.14}$	$-2.81^{+0.13}_{-0.13}$	$-3.19^{+0.57}_{-0.56}$

Reported quantities (and corresponding 1σ uncertainties) are the flux density F_ν in nJy, the UV magnitude (M_{UV}) in magnitudes, the bolometric luminosity (L_{bol}) in 10^{10} Solar luminosity, and UV slopes taking into account all available filters redwards of 2 μm (β_{UV}) or only up to and including F335M ($\hat{\beta}_{\text{UV}}$). Fluxes in available HST and JWST filters are measured with forcepho and within circular 0.3''-diameter apertures (CIRC2), except for MIRI/F770W, as detailed in Photometric measurements. Synthetic photometry in NIRCam filters is directly extracted from the NIRSpec/PRISM spectrum (see Supplementary information). For each of the three different sets of photometry, UV properties (L_{bol} , M_{UV} and β_{UV}) are measured redwards of $\lambda_{\text{obs}} = 2.0 \mu\text{m}$, corresponding to rest-frame wavelengths $\lambda_{\text{emit}} \gtrsim 1500 \text{ \AA}$ at $z = 13$ (see Supplementary information for details). The uncertainty on the UV magnitude (M_{UV}) takes into account a systematic uncertainty of $\Delta z = 0.05$.

Extended Data Table 2 | Emission-line constraints for JADES-GS-z13-1-LA.

Emission line(s)	F (10^{-19} erg s $^{-1}$ cm $^{-2}$)	EW (Å)
Ly α	7.42 ± 1.16	$> 40^*$
He II $\lambda 1640$ Å	< 1.6	< 30
N IV] $\lambda 1483, 1487$ Å	< 2.0	< 29
C IV $\lambda 1548, 1551$ Å	< 1.6	< 27
[O III] $\lambda 1660, 1666$ Å	< 1.2	< 25
N III]	< 1.8	< 43
C III]	< 1.1	< 36
[O II] $\lambda 3727, 3730$ Å	< 0.95	< 42

Presented quantities for each line are the flux and EW from the PRISM spectra. Constraints for undetected lines are presented as 3σ upper limits. N III] refers to the multiplet at 1750 Å, while C III] is shorthand for [C III] $\lambda 1907$ Å, C III] $\lambda 1909$ Å.

*Discussed in more detail in Spectral modelling.

not find a strong wavelength dependency of the morphology. In the F277W filter, which probes rest-frame wavelengths around $\lambda_{\text{emit}} \approx 2000$ Å at $z = 13$, we constrain JADES-GS-z13-1-LA to have a half-light radius of $17.5^{+3.0}_{-1.7}$ mas and a Sérsic index consistent with $n = 1$. This size approaches half the pixel size (i.e. 15 mas) and should hence be treated as an upper limit, given the mosaicing procedure likely introduces artificial smoothing.

To fit to independent dithered NIRCam exposures, we performed further modelling with FORCEPHO (Johnson et al. in prep.), adopting a model with a single intrinsic Sérsic profile and freely varying normalisation in each filter (e.g. refs. ^{65–67}). Importantly, by fitting to the individual exposures FORCEPHO avoids correlated noise between pixels in drizzled mosaic images, enabling us to probe scales smaller than individual pixels. The results are shown in Extended Data Fig. 1, and the resulting photometry is listed in Extended Data Table 1. From this analysis, we find a formal upper limit (84th percentile) on the half-light radius of 5.1 mas. We therefore conclude the imaging data is consistent with the continuum source being unresolved. Based on tests with similarly faint brown dwarf stars that allow the expected systematic uncertainties to be quantified, we conservatively adopt an upper limit on the half-light radius as reported by Robertson et al. ¹⁶ for the F200W filter, $\lesssim 10$ mas or $\lesssim 35$ pc.

Emission-line properties

The emission line at 1.71 μm is clearly and consistently detected across different PRISM data reductions, even when only one of the two individual visits is considered (Supplementary information). We first fit a Gaussian profile to the sigma-clipped spectrum using the corresponding covariance matrix (Supplementary information), which provides a good fit to the data: $\chi^2 = 5.97$ with 5 degrees of freedom (DOF). We obtain a centroid of 1.7084 ± 0.0014 μm and FWHM = 302 ± 18 Å (or $\Delta v \approx 5000$ km s $^{-1}$) that spans 2.4 wavelength bins (120 Å wide at 1.71 μm). We conclude that the line is likely unresolved in the PRISM spectrum and, as expected for compact sources observed with the NIRSpec MSA ⁶⁸, that the spectral

resolution is enhanced by a factor of $\approx 1.5\times$ compared to the resolution curve predicted for a uniformly illuminated micro-shutter.[‡]

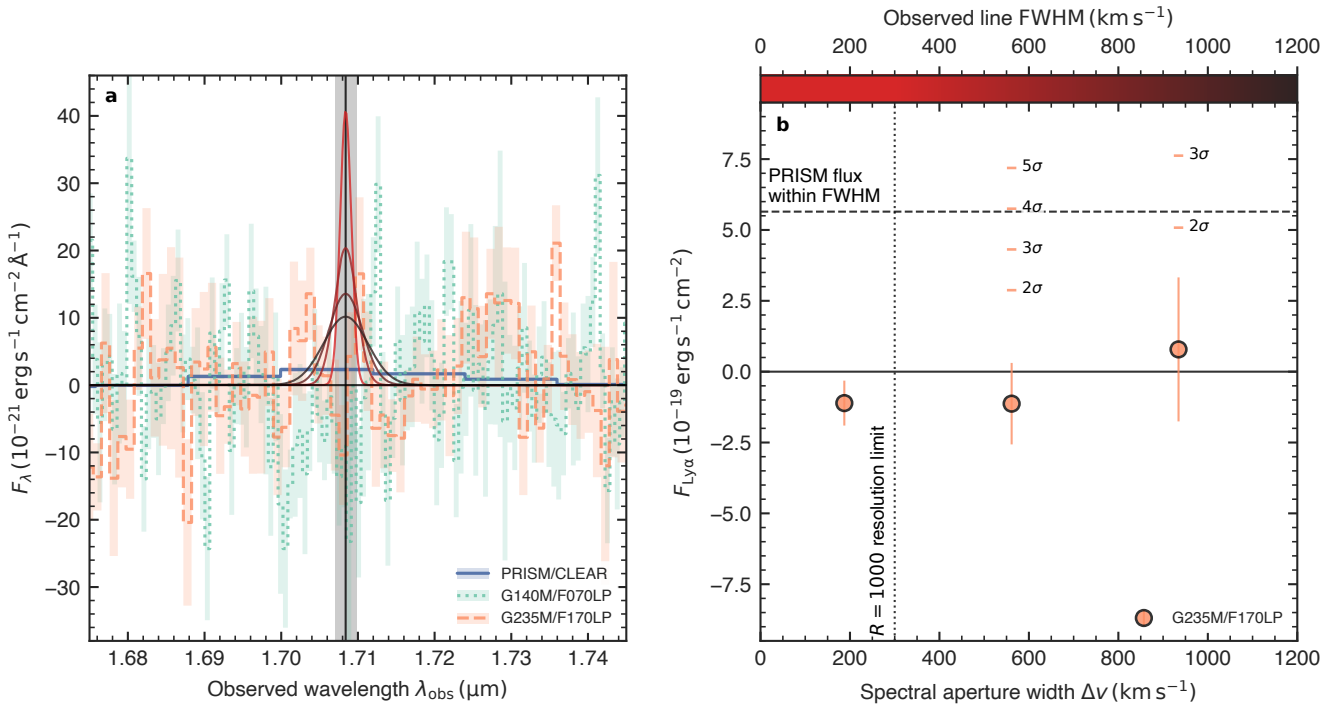
To measure the absolute flux of the line, we first applied a correction to both the sigma-clipped spectrum and the covariance matrix based on the linear FORCEPHO fit found in our path-loss analysis (Supplementary information) to account for additional path losses in the NIRSpec measurements. Directly integrating the corrected PRISM spectrum across the four wavelength bins between 1.69 μm and 1.73 μm (each bin with SNR > 1 ; Supplementary Information), we find a flux of $F = 7.42 \pm 1.16 \times 10^{-19}$ erg s $^{-1}$ cm $^{-2}$ (i.e. the line is detected at SNR = 6.4). We have verified that all different data reductions (see Supplementary information) yield measurements consistent within 1σ . Specifically, the two visits independently confirm the line detection with measured fluxes of $5.77 \pm 1.36 \times 10^{-19}$ erg s $^{-1}$ cm $^{-2}$ and $9.07 \pm 1.80 \times 10^{-19}$ erg s $^{-1}$ cm $^{-2}$, respectively.

The emission line is not detected in the medium-resolution G140M/F070LP or G235M/F170LP spectra, both of which cover 1.71 μm as shown in Extended Data Fig. 2 (though we note the G235M/F170LP transmission drops below 1.7 μm; ref. ¹⁷). To quantify whether this is expected, taking into account their inherently lower sensitivity and relatively short exposure times compared to the PRISM (NIRSpec observations and data reduction), we tested if the observed R1000 spectra are consistent with the line flux measured in the PRISM spectra. Indeed, we find that if the observed line profile is sufficiently broadened (FWHM $\gtrsim 600$ km s $^{-1}$, i.e. well-resolved at $R = 1000$ resolution), it would be below the current sensitivity ($\lesssim 2\sigma$ detection expected; Extended Data Fig. 2).

As discussed further in the Supplementary information, we find it highly unlikely that the emission line at 1.71 μm is due to contamination of the micro-shutter by a foreground source that is aligned with JADES-GS-z13-1-LA by chance and remains undetected in the continuum, given that the continuum emission of JADES-GS-z13-1-LA unambiguously places the source at $z \approx 13$. We have performed the ‘redshift sweep’ analysis detailed in the appendices of Hainline et al. ⁹ and Carniani et al. ⁵, in which the inferred the one-sided p -value for a set of different emission lines is combined to yield the statistical significance of a potential spectroscopic confirmation at a given redshift. The effectiveness of this method is illustrated by the case of GS-z14-0, where the most likely redshift was revealed ⁵ to be $z = 14.178$ (combined $p = 0.0072$) mainly based on a 3.6σ detection of C III]. This redshift, consistent within the uncertainty determined from fitting the Ly α break profile with DLA absorption, was later independently confirmed via the detection ^{21, 69} of the [O III] 88 μm emission line by ALMA. In the case of JADES-GS-z13-1-LA, the redshift sweep was performed across a range of $\Delta z = 0.2$ centred on $z = 13.0$, which however did not show any significant line detections.

Upper limits on the flux and EW for other, undetected lines at $z = 13$ are therefore determined from integrating the covariance matrix across 3 PRISM wavelength bins, taking into account any residual flux after having subtracted a power-law model continuum (Spectral modelling). The resulting limits, summarised in Extended Data Table 2, are consistent with findings on most other $z > 10$ galaxies observed by JWST, which generally have revealed these lines to be relatively weak ^{3, 4, 6, 23, 24}.

[‡] Available at <https://jwst-docs.stsci.edu/jwst-near-infrared-spectrograph/nirspec-instrumentation/nirspec-dispersers-and-filters>.



Extended Data Fig. 2 | Medium-resolution (R1000) grating spectra of JADES-GS-z13-1-LA. **a**, Coloured lines represent observed spectra in different grating-filter modes, as obtained from the sigma-clipping procedure (Supplementary information). Specifically, we show the G140M/F070LP (turquoise, dotted) and G235M/F170LP (orange, dashed) spectra compared to the low-resolution PRISM spectrum (dark blue). Shading represents a 1σ uncertainty on all components of the figure. Solid curves represent emission-line profiles at increasing widths (according to the colourbar in panel b), starting from the $R = 1000$ resolution limit and having matched the flux and central wavelength ($1.708 \mu\text{m}$; indicated by a vertical black line) to the values measured from the PRISM spectrum (see Emission-line properties). **b**, Measured Ly α flux in an increasingly wide spectral aperture centred on $1.708 \mu\text{m}$ in G235M/F170LP are shown by circles with 1σ error bars, none of which show a significant detection. This is consistent with the less sensitive G140M/F070LP measurements (not shown here for clarity). A horizontal dashed line shows the measured PRISM line flux contained within the FWHM of a Gaussian profile (76%), while a vertical dotted line indicates the limiting $R = 1000$ resolution. This illustrates that if the emission line is well resolved ($\text{FWHM} \gtrsim 600 \text{ km s}^{-1}$), it would fall below the nominal noise level of the R1000 gratings (cf. annotated 2σ and 4σ levels).

Spectral modelling

To gain insight into the Ly α emission and absorption properties of JADES-GS-z13-1-LA, we model the observed spectrum with a simple framework in which Ly α and continuum emission produced inside the central galaxy are subject to (damping-wing) absorption arising in intervening neutral hydrogen in dense absorbing systems and/or the IGM. We emphasise that the aim of this model is not to be as physically detailed as possible, which would involve performing simulations including three-dimensional radiative transfer coupled to the hydrodynamics of the gas (requiring the relevant feedback processes to be accurately modelled), but rather to constrain the basic physical properties that JADES-GS-z13-1-LA must possess to explain the observations.

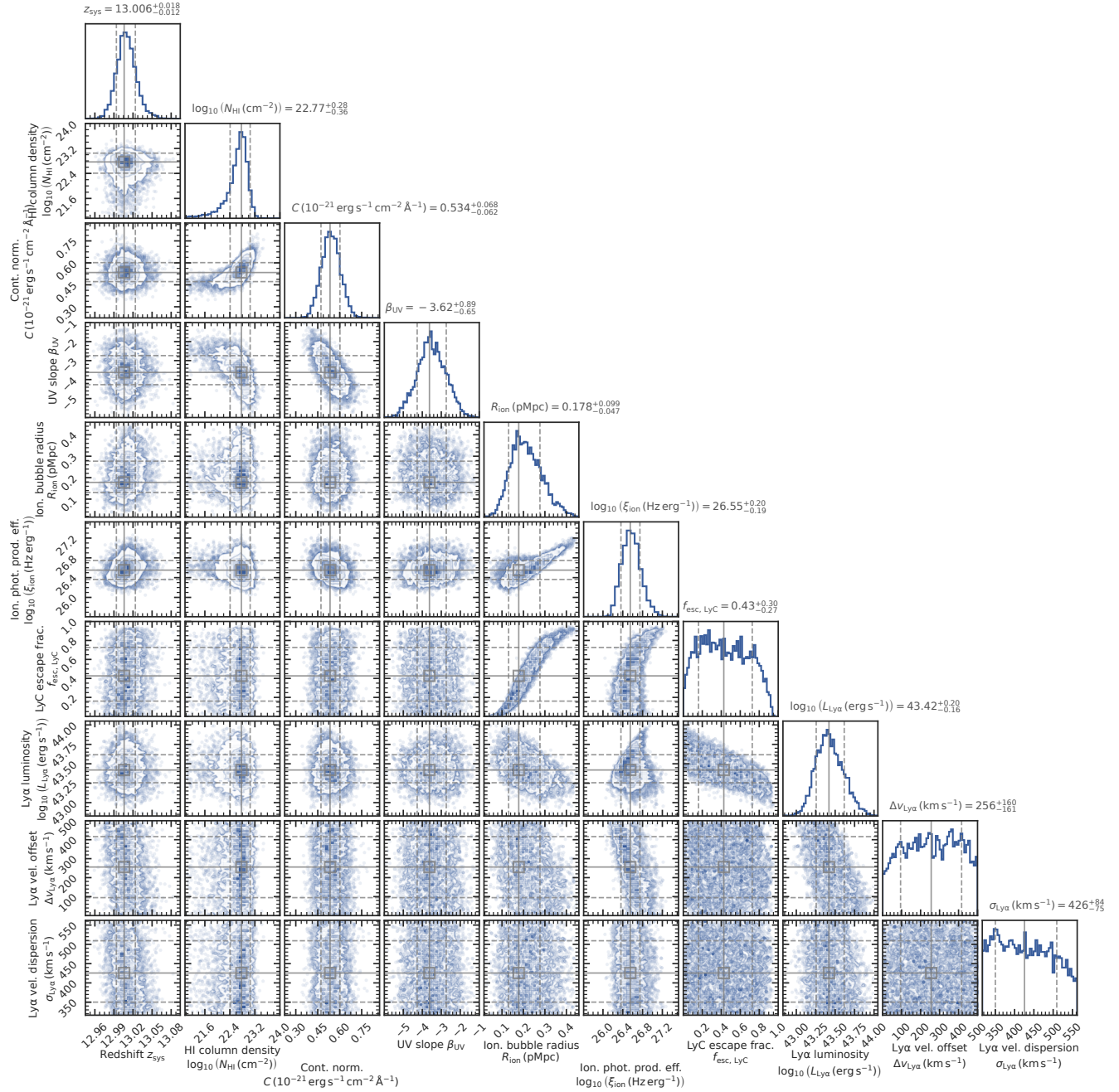
As we expect the Ly α line to be redshifted with respect to the systemic redshift of the galaxy (potentially already as Ly α emerges from the galaxy or otherwise resulting from processing by the neutral IGM^{70,71}) and no other emission lines are detected (Emission-line properties), this quantity (z_{sys}) is not precisely known and is a free parameter in this model. To remain agnostic about the nature of the ionising source and to avoid the intrinsic limitations of standard SPS models in reproducing very blue UV continua (Supplementary information), the continuum emission is modelled as a power law, $F_\lambda \propto \lambda^{\beta_{\text{UV}}}$, by default. This introduces two more free parameters

in the model, the UV slope β_{UV} and a normalisation (at rest-frame wavelength of $\lambda_{\text{emit}} = 1500 \text{ \AA}$).

To reproduce the smooth Ly α break seen in the continuum, we allow the continuum emission to be impacted by DLA absorption parametrised by the neutral hydrogen column density N_{H_1} as in refs.^{6,9}. The Ly α emission is explicitly not attenuated by this absorption, as this would completely extinguish the line.[§] As discussed in the main text, this would require a specific geometrical configuration such that the Ly α emission is not strongly absorbed, however Ly α emission superimposed on DLA troughs has been observed in galaxy spectra, suggesting that these geometries exist^{45,46}. The absorption cross section of neutral hydrogen is based on the Voigt profile approximation given by Tasitsiomi⁷², with a quantum-mechanical correction provided by Bach & Lee⁷³. Since we find that the redshift of the foreground DLA system (when freely varied; e.g. ref.⁷⁴) prefers a solution close to the systemic redshift, $z_{\text{DLA}} \approx z_{\text{sys}}$, for simplicity we fix $z_{\text{DLA}} = z_{\text{sys}}$ in the following.

Alternatively, we considered the case where the observed spectrum is dominated by the 2γ continuum, which has a fixed shape⁷⁵

[§] Since the attenuated continuum tends to zero at the wavelength of Ly α , we calculate the line EW according to the unattenuated continuum, which is effectively equivalent to measuring the continuum level via the photometry.



Extended Data Fig. 3 | Posterior distributions from spectral modelling of the observed spectrum of JADES-GS-z13-1-LA. The small panels show inter-dependencies between all 8 parameters freely varied in the model (Extended Data Table 3). Additionally, we include the physical radius of the ionised bubble (R_{ion}) and Ly α luminosity ($L_{\text{Ly}\alpha}$), which are not independently varied but instead are determined by the other parameters (see Spectral modelling).

and thus only requires one free parameter, the normalisation. As a third variant, we considered a combination consisting of a power-law continuum (using the same parametrisation as above) and a full nebular emission spectrum, which in addition to the 2γ continuum and the Ly α line also contains the free-bound (and free-free) components. The nebular emission in this case was computed with the PYNEB code⁷⁶, which however requires assuming the gas temperature and density. We opted for $T = 20\,000\text{ K}$ and $n = 100\text{ cm}^{-3}$ respectively, where the 2γ continuum is dominant contributor to the

wavelength range considered here⁷⁷. The choice for this relatively low density is motivated by the fact that the free-bound (and free-free) components mainly contribute at longer wavelengths and would have to be subdominant to reproduce the very steep UV slope. In this multi-component ('self-consistent') model, we tied the continuum normalisation to the strength of the Ly α line, thereby self-consistently scaling the continuum according to the production rate and escape fraction of LyC photons discussed below.

Following refs. 11, 78, IGM transmission was calculated with the

Extended Data Table 3 | Spectral model parameters, prior distributions, and best-fitting values.

Parameter	(Logarithmic) unit	Type	Prior	Min.	Max.	Default (power law)	Pure 2γ	Self- consistent	Fixed $R_{\text{ion}} = 0$
z_{sys}		Varied	Uniform	12.85	13.1	$13.01^{+0.02}_{-0.01}$	$13.01^{+0.01}_{-0.02}$	$13.01^{+0.02}_{-0.02}$	$12.99^{+0.02}_{-0.02}$
$\log_{10}(N_{\text{H}})$	cm^{-2}	Varied	Uniform	19	24	$22.77^{+0.28}_{-0.36}$	$19.58^{+1.10}_{-0.41}$	$22.60^{+0.51}_{-1.24}$	$22.79^{+0.31}_{-0.40}$
C	$10^{-21} \text{ erg s}^{-1} \text{ cm}^{-2} \text{ \AA}^{-1}$	Varied	Uniform	0	1	$0.534^{+0.068}_{-0.062}$	$0.444^{+0.031}_{-0.030}$	$0.215^{+0.104}_{-0.056}$ *	$0.546^{+0.063}_{-0.081}$
β_{UV}		Varied	Uniform	-6	-1	$-3.62^{+0.89}_{-0.65}$	-	$-5.52^{+1.19}_{-0.43}$	$-3.60^{+0.93}_{-0.72}$
R_{ion}	pMpc	Coupled/fixed	-	-	-	$0.178^{+0.099}_{-0.047}$	$0.177^{+0.102}_{-0.057}$	$0.253^{+0.092}_{-0.074}$	0^{\dagger}
$\log_{10}(\xi_{\text{ion}})$	Hz erg^{-1}	Varied	Uniform	24	28	$26.55^{+0.20}_{-0.19}$	$26.62^{+0.17}_{-0.22}$	$27.00^{+0.23}_{-0.32}$ *	$26.60^{+0.09}_{-0.14}$
$f_{\text{esc, LyC}}$		Varied/fixed	Uniform	0	1	$0.43^{+0.30}_{-0.27}$	$0.42^{+0.34}_{-0.26}$	$0.73^{+0.14}_{-0.26}$	0^{\dagger}
$L_{\text{Ly}\alpha}$	$10^{43} \text{ erg s}^{-1}$	Coupled	-	-	-	$2.6^{+1.5}_{-0.8}$	$2.6^{+1.5}_{-0.9}$	$1.6^{+0.3}_{-0.3}$	$5.5^{+1.9}_{-0.9}$
$\text{EW}_{\text{Ly}\alpha, \text{intr}}$	\AA	Coupled	-	-	-	691^{+467}_{-254}	-‡	704^{+541}_{-289}	1375^{+591}_{-420}
$\text{EW}_{\text{Ly}\alpha, \text{obs}}$	\AA	Coupled	-	-	-	43^{+15}_{-11}	-‡	67^{+43}_{-23}	41^{+16}_{-11}
$f_{\text{esc, Ly}\alpha}$		Coupled	-	-	-	$0.063^{+0.026}_{-0.023}$	$0.063^{+0.027}_{-0.022}$	$0.095^{+0.025}_{-0.020}$	$0.030^{+0.008}_{-0.007}$
$\Delta v_{\text{Ly}\alpha, \text{int}}$	km s^{-1}	Varied	Uniform	0	500	256^{+160}_{-161}	257^{+161}_{-163}	379^{+83}_{-150}	391^{+74}_{-111}
$\Delta v_{\text{Ly}\alpha, \text{obs}}$	km s^{-1}	Coupled	-	-	-	694^{+299}_{-299}	603^{+299}_{-269}	638^{+359}_{-299}	930^{+329}_{-299}
$\sigma_{\text{Ly}\alpha}$	km s^{-1}	Varied	Log-uniform	$10^{2.5}$	$10^{2.75}$	426^{+84}_{-75}	430^{+82}_{-77}	436^{+83}_{-81}	457^{+73}_{-86}
χ^2						168.1	175.6	171.4	168.4
DOF						119	120	119	120

Model parameters are the systemic redshift (z_{sys}), DLA neutral hydrogen column density (N_{H}), power-law continuum normalisation (C) and slope (β_{UV}), ionising-photon production efficiency (ξ_{ion}) and escape fraction ($f_{\text{esc, LyC}}$), and the peak velocity offset ($\Delta v_{\text{Ly}\alpha, \text{int}}$) and intrinsic velocity dispersion ($\sigma_{\text{Ly}\alpha}$) of Ly α line profile emerging from the galaxy. Additional reported parameters are the ionised bubble radius (R_{ion}), Ly α luminosity ($L_{\text{Ly}\alpha}$), Ly α EW as it emerges from the galaxy ($\text{EW}_{\text{Ly}\alpha, \text{intr}}$) and as it is observed (i.e. after IGM transmission; $\text{EW}_{\text{Ly}\alpha, \text{obs}}$), Ly α escape fraction ($f_{\text{esc, Ly}\alpha}$), and the observed Ly α velocity offset ($\Delta v_{\text{Ly}\alpha, \text{obs}}$), which are not freely varied but derived from the main parameters. Best-fitting values (uncertainties) are the median (16th and 84th percentiles) of the posterior distribution under the default (power-law) model, a model with pure two-photon continuum (2γ), a self-consistent model incorporating power-law and nebular-emission components, and a power-law model where $R_{\text{ion}} = 0$ (for details, see Spectral modelling).

* (Relative to the) power-law continuum only.

† Value is fixed in this model.

‡ The 2γ continuum tends to zero approaching the wavelength of Ly α .

patchy reionisation model presented in Mason & Gronke⁷⁹, integrating along the trajectory of a photon which starts in an ionised bubble of radius R_{ion} located in an otherwise neutral IGM (see also refs. 80,81). Following Mason & Gronke⁷⁹, we assume the gas in the ionised bubble to be highly ionised (residual neutral fraction fixed at $x_{\text{H}} = 10^{-8}$) and have $T = 10^4 \text{ K}$, whereas the neutral IGM is at $T = 1 \text{ K}$. The gas in both media is assumed to be at mean cosmic density (i.e. to have $\bar{n}_{\text{H}} \approx 5.25 \times 10^{-4} \text{ cm}^{-3}$ at $z = 13$), and be at rest with respect to the central source. We fixed the global neutral hydrogen fraction of the IGM (i.e. outside the ionised bubble⁷⁸) to $\bar{x}_{\text{H}} = 1$, motivated by various types of evidence which consistently indicate that globally, the Universe is still highly neutral well below redshift $z = 13$ (e.g. refs. 82,83).

We self-consistently model the size of the ionised bubble by considering the production rate and escape fraction of hydrogen-ionising photons of the central galaxy. As in Witstok et al.¹¹, we define $\xi_{\text{ion}} \equiv \dot{N}_{\text{ion}}/L_{\nu, \text{UV}}$, where \dot{N}_{ion} is the production rate of ionising photons and $L_{\nu, \text{UV}}$ is the luminosity density (in units of $\text{erg s}^{-1} \text{ Hz}^{-1}$) of the intrinsic continuum of the ionising source at $\lambda_{\text{emit}} = 1500 \text{ \AA}$. In the case of the multi-component model in particular, $L_{\nu, \text{UV}}$ is taken to be the value of the power-law continuum at 1500 \AA such that ξ_{ion} reflects the intrinsic value. The rate of ionising photons leaking from the galaxy at a given production efficiency ξ_{ion} is modulated by the LyC escape fraction, $f_{\text{esc, LyC}}$. In a given model

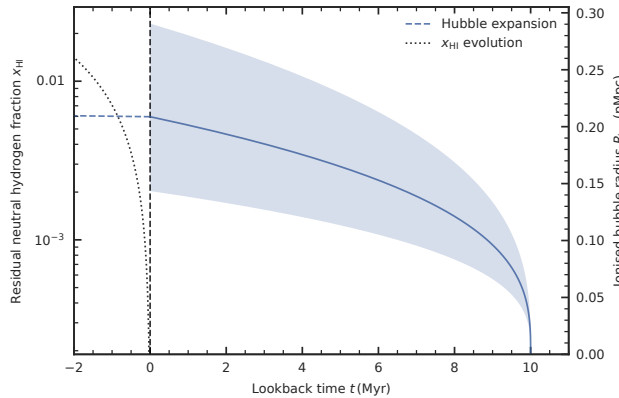
instance, we therefore begin by deriving the rate of ionising photons escaping the galaxy via (e.g. refs. 26, 84–86)

$$\dot{N}_{\text{ion, esc}} = f_{\text{esc, LyC}} \dot{N}_{\text{ion}} = f_{\text{esc, LyC}} \xi_{\text{ion}} L_{\nu, \text{UV}}. \quad (1)$$

To calculate the bubble radius R_{ion} , we then numerically integrate equation (3) in Cen & Haiman⁸⁰, describing the time evolution of $R_{\text{ion}}(t)$ to obey

$$\frac{dR_{\text{ion}}^3}{dt} = 3H(z)R_{\text{ion}}^3 + \frac{3\dot{N}_{\text{ion, esc}}}{4\pi\bar{n}_{\text{H}}} - C_{\text{H II}}\bar{n}_{\text{H}}\alpha_{\text{B}}R_{\text{ion}}^3, \quad (2)$$

thereby taking into account the effect of the expansion of the Universe parametrised by the Hubble parameter $H(z)$ and recombinations within the ionised bubble, for which we assume a clumping factor for ionised gas of $C_{\text{H II}} = 3$ (e.g. ref. 87) and case-B recombination rate α_{B} at 20 000 K as given by Draine⁸⁸. The typical recombination timescale at $z = 13$, $(C_{\text{H II}}\bar{n}_{\text{H}}\alpha_{\text{B}})^{-1} \approx 140 \text{ Myr}$, indicates that JADES-GS-z13-1-LA as an ionising source could quickly ionise its surroundings before recombinations are able to restore balance. As illustrated in Extended Data Fig. 4, showing the time evolution of R_{ion} in the default model, the bubble radius can reach $R_{\text{ion}} \approx 0.1 \text{ pMpc}$ over a timescale of only 1 Myr. We note that when the supply of LyC photons ceases, the residual neutral hydrogen fraction does rapidly increase due to the high density at $z = 13$ ($x_{\text{H}} \approx 0.01$ after 1 Myr),



Extended Data Fig. 4 | Modelled ionised bubble size evolution. The right axis shows the physical radius of the ionised bubble R_{ion} , whose evolution as a function of lookback time t is governed by equation (2). The solid line shows the median among the posterior distribution of the default model, shading represents 1σ uncertainty (16th to 84th percentile). The dashed line illustrates the Hubble expansion rate if the bubble remains unchanged from $t = 0$ onwards, showing this effect has little impact over the timescale relevant to our analysis. The dotted line shows how the neutral hydrogen fraction within the bubble (left axis) would evolve without additional ionising photons.

implying that for an ionised bubble to have a significant transmission-enhancing effect redwards of the systemic Ly α wavelength⁷⁹ it must be actively maintained. Here, we integrate until reaching a fiducial age of $t = 10$ Myr, having verified that changing this assumption has little impact on our findings as a result of the sub-linear scaling $R_{\text{ion}} \propto t^{1/3}$ (in the absence of recombinations and the Hubble flow). We additionally considered an alternative model identical to the default power-law one, but where we fix $R_{\text{ion}} = 0$ (i.e. $f_{\text{esc, LyC}} = 0$).

Finally, we determine the intrinsic Ly α luminosity resulting from recombinations by considering the number of ionising photons that are absorbed within the galaxy and reprocessed into Ly α . Similarly to the above, the effective rate of LyC photons contributing to the recombination rate within the galaxy (\dot{N}_{rec}) follows from the product of the intrinsic production rate \dot{N}_{ion} and absorbed fraction (one minus the escape fraction) of ionising photons. This is multiplied by the fraction of (case-B) recombination events that result in the emission of a Ly α photon, $f_{\text{rec, B}}$ (see e.g. ref. ⁸⁹), to arrive at the emission rate of Ly α photons, and hence the Ly α luminosity (i.e. the emission rate times the energy of a Ly α photon),

$$L_{\text{Ly}\alpha} = \dot{N}_{\text{rec, B}} E_{\text{Ly}\alpha} = (1 - f_{\text{esc, LyC}}) \xi_{\text{ion}} L_{\nu, \text{UV}} f_{\text{rec, B}} E_{\text{Ly}\alpha}. \quad (3)$$

We used $f_{\text{rec, B}} (T = 20\,000 \text{ K}) = 0.647$ based on the prescription by Dijkstra ⁹⁰, noting it depends only weakly on temperature ⁹¹ and that case A would lead to an unaccounted increase in $f_{\text{esc, LyC}}$. Under the very conservative assumptions of no IGM absorption at all and $f_{\text{esc, LyC}} = 0$, equation (3) places a lower limit on the LyC production efficiency via the observed Ly α luminosity relative to the continuum, yielding $\xi_{\text{ion}} \gtrsim 10^{25.1} \text{ Hz erg}^{-1}$ ($10^{25.4} \text{ Hz erg}^{-1}$ under case A). The Ly α line, as it emerges from the galaxy, is modelled as a Gaussian profile with a given velocity dispersion $\sigma_{\text{Ly}\alpha}$, which is shifted in velocity space at a given offset from the systemic redshift, $\Delta v_{\text{Ly}\alpha, \text{int}}$, and normalised to the Ly α luminosity derived as described above.

Radiative transfer calculations predict a large variety of Ly α spec-

tral profiles may emerge from galaxies ^{92,93}, but galactic outflows typically cause systematically redshifted components ^{94,95}, as seen ubiquitously at high redshift ^{70,71,96–99}. While the emergent Ly α spectral profile is fundamentally unknown at $z \gtrsim 7$ due to the asymmetric IGM transmission on the blue side ^{78,79}, some clues are given by the non-detection of the line in the R1000 spectra. If the line were unresolved at a resolution of $R \approx 1000$, that is $\text{FWHM} \lesssim 300 \text{ km s}^{-1}$, we would have likely seen a marginal detection (Extended Data Fig. 2). Instead, the line profile likely contains a prominent red, broad component to allow for sufficient transmission of Ly α flux at $z = 13$ even in the presence of an ionised bubble (Fig. 2). We note that due to the IGM transmission, the peak of the intrinsic line profile at velocity offset $\Delta v_{\text{Ly}\alpha, \text{int}}$ with respect to systemic effectively gets further redshifted to a velocity offset of $\Delta v_{\text{Ly}\alpha, \text{obs}}$.

We employed the PYMULTINEST ¹⁰⁰ implementation of the multimodal nested-sampling algorithm MULTINEST ¹⁰¹ to perform a Bayesian fitting routine [¶] to the sigma-clipped PRISM spectrum and corresponding covariance matrix (see Supplementary information) from $1.609 \mu\text{m}$ up to $2.897 \mu\text{m}$ (127 wavelength bins), or $1150 \text{ \AA} \lesssim \lambda_{\text{emit}} \lesssim 2000 \text{ \AA}$ at $z = 13$. Before fitting, as in Emission-line properties we corrected the NIRSpec measurements for additional path losses. Meanwhile, the model spectrum is convolved with the PRISM resolution curve predicted for a uniformly illuminated micro-shutter, enhanced by a factor of 1.5 based on the measured width of the Ly α line in the PRISM (see Emission-line properties). As detailed in Jakobsen et al. (in prep.), the goodness of fit statistic χ^2 is calculated as the matrix product

$$\chi^2 = \mathbf{R}^T \boldsymbol{\Sigma}^{-1} \mathbf{R}, \quad (4)$$

where $\boldsymbol{\Sigma}^{-1}$ is the inverted covariance matrix and the i^{th} element of the vector \mathbf{R} is given as the difference between observed flux density in the i^{th} wavelength bin ($F_{\lambda, i}^{\text{obs}}$) and the modelled one ($F_{\lambda, i}^{\text{model}}$),

$$R_i = F_{\lambda, i}^{\text{obs}} - F_{\lambda, i}^{\text{model}}. \quad (5)$$

The model log-likelihood ℓ is calculated assuming the observed data are normally distributed around the model, $\ell = -\frac{1}{2} \chi^2$. All model parameters, adopted prior distributions, and resulting best-fitting values are summarised in Extended Data Table 3. The posterior distributions for the default model are shown in Extended Data Fig. 3.

While the multi-component self-consistent model has a slightly higher χ^2 (171.4) than the default power-law model ($\chi^2 = 168.1$), interestingly it favours a high LyC escape fraction ($f_{\text{esc, LyC}} = 0.73^{+0.14}_{-0.26}$) to suppress the nebular continuum, much like the SPS model fits (Supplementary information). Indeed, fixing $R_{\text{ion}} = 0$ in the self-consistent model (results not included here) yields a significantly poorer fit ($\chi^2 = 183.1$), as this overpredicts the continuum tied to the strong Ly α line. Moreover, the intrinsic Ly α flux required for the $R_{\text{ion}} = 0$ power-law model is discrepant at a 4.5σ level with the MIRI/F770W non-detection (Photometric measurements).

Data availability

The NIRCam data that support the findings of this study are publicly available at <https://archive.stsci.edu/hlsp/jades>. The reduced spectra that support the findings of this study are publicly available at <https://doi.org/10.5281/zenodo.14714293>.

[¶] Code available at https://github.com/joriswitstok/lyman-alpha_absorption.

Code availability

The code used for the Spectral modelling fitting routine is available at https://github.com/joriswitstok/lymanalpha_absorption. The ASTROPY^{102,103} software suite is publicly available, as is BAGPIPES¹⁰⁴, BEAGLE¹⁰⁵, CLOUDY¹⁰⁶, EMCEE¹⁰⁷, FORCEPHO¹⁰⁸, MULTINEST¹⁰¹, PYMULTINEST¹⁰⁰, PYNEB⁷⁶, the SciPy library¹⁰⁹, its packages NUMPY¹¹⁰ and MATPLOTLIB¹¹¹, and SPECTRES¹¹².

References (continued)

52. Planck Collaboration et al., 2020. Planck 2018 results. VI. Cosmological parameters, *A&A*, **641**, A6
53. Oke J. B., Gunn J. E., 1983. Secondary standard stars for absolute spectrophotometry., *ApJ*, **266**, 713
54. Helton J. M., et al., 2024. JWST/MIRI photometric detection at $7.7 \mu\text{m}$ in a galaxy at $z > 14$, p. [arXiv:2405.18462](https://arxiv.org/abs/2405.18462) [arXiv:2405.18462](https://arxiv.org/abs/2405.18462)
55. Rieke M. J., et al., 2023. JADES Initial Data Release for the Hubble Ultra Deep Field: Revealing the Faint Infrared Sky with Deep JWST NIRCam Imaging, *ApJS*, **269**, 16
56. Bunker A. J., et al., 2024. JADES NIRSpec initial data release for the Hubble Ultra Deep Field: Redshifts and line fluxes of distant galaxies from the deepest JWST Cycle 1 NIRSpec multi-object spectroscopy, *A&A*, **690**, A288
57. D'Eugenio F., et al., 2024. JADES Data Release 3 – NIRSpec/MSA spectroscopy for 4,000 galaxies in the GOODS fields, p. [arXiv:2404.06531](https://arxiv.org/abs/2404.06531) [arXiv:2404.06531](https://arxiv.org/abs/2404.06531)
58. Böker T., et al., 2023. In-orbit Performance of the Near-infrared Spectrograph NIRSpec on the James Webb Space Telescope, *PASP*, **135**, 038001
59. Giavalisco M., et al., 2004. The Great Observatories Origins Deep Survey: Initial Results from Optical and Near-Infrared Imaging, *ApJ*, **600**, L93
60. Illingworth G., et al., 2016. The Hubble Legacy Fields (HLF-GOODS-S) v1.5 Data Products: Combining 2442 Orbits of GOODS-S/CDF-S Region ACS and WFC3/IR Images, p. [arXiv:1606.00841](https://arxiv.org/abs/1606.00841) [arXiv:1606.00841](https://arxiv.org/abs/1606.00841)
61. Ferruit P., et al., 2022. The Near-Infrared Spectrograph (NIRSpec) on the James Webb Space Telescope. II. Multi-object spectroscopy (MOS), *A&A*, **661**, A81
62. Rauscher B. J., et al., 2017. Improved Reference Sampling and Subtraction: A Technique for Reducing the Read Noise of Near-infrared Detector Systems, *PASP*, **129**, 105003
63. Sérsic J. L., 1963. Influence of the atmospheric and instrumental dispersion on the brightness distribution in a galaxy, *Boletín de la Asociación Argentina de Astronomía La Plata Argentina*, **6**, 41
64. Pasha I., Miller T. B., 2023. pysersic: A Python package for determining galaxy structural properties via Bayesian inference, accelerated with jax, *The Journal of Open Source Software*, **8**, 5703
65. Robertson B. E., et al., 2023. Identification and properties of intense star-forming galaxies at redshifts $z > 10$, *Nature Astronomy*, **7**, 611
66. Tacchella S., et al., 2023. JADES Imaging of GN-z11: Revealing the Morphology and Environment of a Luminous Galaxy 430 Myr after the Big Bang, *ApJ*, **952**, 74
67. Baker W. M., et al., 2024. A core in a star-forming disc as evidence of inside-out growth in the early Universe, *Nature Astronomy*,
68. De Graaff A., et al., 2024. Ionised gas kinematics and dynamical masses of $z \gtrsim 6$ galaxies from JADES/NIRSpec high-resolution spectroscopy, *A&A*, **684**, A87
69. Schouws S., et al., 2024. Detection of [OIII]88 μm in JADES-GS-z14-0 at $z=14.1793$, p. [arXiv:2409.20549](https://arxiv.org/abs/2409.20549) [arXiv:2409.20549](https://arxiv.org/abs/2409.20549)
70. Tang M., et al., 2024a. Ly α emission in galaxies at $z \approx 5 - 6$: new insight from JWST into the statistical distributions of Ly α properties at the end of reionization, *MNRAS*, **531**, 2701
71. Tang M., et al., 2024b. Ly α Emission Line Profiles of Extreme [O III]- emitting Galaxies at $z \gtrsim 2$: Implications for Ly α Visibility in the Reionization Era, *ApJ*, **972**, 56
72. Tasitsiomi A., 2006. Ly α Radiative Transfer in Cosmological Simulations and Application to a $z \approx 8$ Ly α Emitter, *ApJ*, **645**, 792
73. Bach K., Lee H.-W., 2015. Accurate Ly α scattering cross-section and red damping wing in the reionization epoch, *MNRAS*, **446**, 264
74. Terp C., et al., 2024. Uncovering the physical origin of the prominent Lyman- α emission and absorption in GS9422 at $z = 5.943$, *A&A*, **690**, A70
75. Spitzer Jr. L., Greenstein J. L., 1951. Continuous Emission from Planetary Nebulae, *ApJ*, **114**, 407
76. Luridiana V., Morisset C., Shaw R. A., 2015. PyNeb: a new tool for analyzing emission lines. I. Code description and validation of results, *A&A*, **573**, A42
77. Schirmer M., 2016. NEBULAR: A Simple Synthesis Code for the Hydrogen and Helium Nebular Spectrum, *PASP*, **128**, 114001
78. Witstok J., et al., 2024. Inside the bubble: exploring the environments of reionisation-era Lyman- α emitting galaxies with JADES and FRESCO, *A&A*, **682**, A40
79. Mason C. A., Gronke M., 2020. Measuring the properties of reionized bubbles with resolved Ly α spectra, *MNRAS*, **499**, 1395
80. Cen R., Haiman Z., 2000. Quasar Strömgren Spheres Before Cosmological Reionization, *ApJ*, **542**, L75
81. Mesinger A., Haiman Z., Cen R., 2004. Probing the Reionization History Using the Spectra of High-Redshift Sources, *ApJ*, **613**, 23
82. Mason C. A., et al., 2019. Inferences on the timeline of reionization at $z \sim 8$ from the KMOS Lens-Amplified Spectroscopic Survey, *MNRAS*, **485**, 3947
83. Tang M., Stark D. P., Topping M. W., Mason C., Ellis R. S., 2024. JWST/NIRSpec Observations of Lyman α Emission in Star-forming Galaxies at $6.5 \lesssim z \lesssim 13$, *ApJ*, **975**, 208
84. Robertson B. E., et al., 2013. New Constraints on Cosmic Reionization from the 2012 Hubble Ultra Deep Field Campaign, *ApJ*, **768**, 71
85. Finkelstein S. L., et al., 2019. Conditions for Reionizing the Universe with a Low Galaxy Ionizing Photon Escape Fraction, *ApJ*, **879**, 36
86. Naidu R. P., et al., 2020. Rapid Reionization by the Oligarchs: The Case for Massive, UV-bright, Star-forming Galaxies with High Escape Fractions, *ApJ*, **892**, 109
87. Pawlik A. H., Schaye J., van Scherpenzeel E., 2009. Keeping the Universe ionized: photoheating and the clumping factor of the high-redshift intergalactic medium, *MNRAS*, **394**, 1812
88. Draine B. T., 2011. Physics of the Interstellar and Intergalactic Medium. Princeton University Press
89. Witstok J., Puchwein E., Kulkarni G., Smit R., Haehnelt M. G., 2021. Prospects for observing the low-density cosmic web in Lyman- α emission, *A&A*, **650**, A98
90. Dijkstra M., 2014. Ly α Emitting Galaxies as a Probe of Reionisation, *Publ. Astron. Soc. Australia*, **31**, e040

91. Osterbrock D. E., Ferland G. J., 2006. Astrophysics of gaseous nebulae and active galactic nuclei. University Science Books (Sausalito, Calif.)
92. Gronke M., Dijkstra M., 2016. Lyman- α Spectra from Multi-phase Outflows, and their Connection to Shell Models, *ApJ*, **826**, 14
93. Blaizot J., et al., 2023. Simulating the diversity of shapes of the Lyman- α line, *MNRAS*, **523**, 3749
94. Verhamme A., Schaerer D., Maselli A., 2006. 3D Ly α radiation transfer. I. Understanding Ly α line profile morphologies, *A&A*, **460**, 397
95. Verhamme A., Schaerer D., Atek H., Tapken C., 2008. 3D Ly α radiation transfer. III. Constraints on gas and stellar properties of $z \sim 3$ Lyman break galaxies (LBG) and implications for high- z LBGs and Ly α emitters, *A&A*, **491**, 89
96. Mason C. A., et al., 2018. The Universe Is Reionizing at $z \sim 7$: Bayesian Inference of the IGM Neutral Fraction Using Ly α Emission from Galaxies, *ApJ*, **856**, 2
97. Tang M., et al., 2021. Lyman-alpha spectroscopy of extreme [O III] emitting galaxies at $z \approx 2-3$: implications for Ly α visibility and LyC leakage at $z > 6$, *MNRAS*, **503**, 4105
98. Witstok J., et al., 2021. Assessing the sources of reionization: a spectroscopic case study of a 30 \times lensed galaxy at $z \approx 5$ with Ly α , C IV, Mg II, and [Ne III], *MNRAS*, **508**, 1686
99. Matthee J., et al., 2021. The X-SHOOTER Lyman α survey at $z = 2$ (XLS-z2) I: what makes a galaxy a Lyman α emitter?, *MNRAS*, **505**, 1382
100. Buchner J., et al., 2014. X-ray spectral modelling of the AGN obscuring region in the CDFS: Bayesian model selection and catalogue, *A&A*, **564**, A125
101. Feroz F., Hobson M. P., Bridges M., 2009. MULTINEST: an efficient and robust Bayesian inference tool for cosmology and particle physics, *MNRAS*, **398**, 1601
102. Astropy Collaboration et al., 2013. Astropy: A community Python package for astronomy, *A&A*, **558**, A33
103. Astropy Collaboration et al., 2018. The Astropy Project: Building an Open-science Project and Status of the v2.0 Core Package, *AJ*, **156**, 123
104. Carnall A. C., McLure R. J., Dunlop J. S., Davé R., 2018. Inferring the star formation histories of massive quiescent galaxies with BAGPIPES: evidence for multiple quenching mechanisms, *MNRAS*, **480**, 4379
105. Chevallard J., Charlot S., 2016. Modelling and interpreting spectral energy distributions of galaxies with BEAGLE, *MNRAS*, **462**, 1415
106. Ferland G. J., et al., 2017. The 2017 Release Cloudy, *Rev. Mex. Astron. Astrofis.*, **53**, 385
107. Foreman-Mackey D., Hogg D. W., Lang D., Goodman J., 2013. emcee: The MCMC Hammer, *PASP*, **125**, 306
108. Baldwin J. O., et al., 2024. forcepho: Generative modeling galaxy photometry for JWST. Astrophysics Source Code Library, record ascl:2410.006
109. Jones E., Oliphant T., Peterson P., et al., 2001. SciPy: Open source scientific tools for Python. <http://www.scipy.org/>
110. Van der Walt S., Colbert S. C., Varoquaux G., 2011. The NumPy Array: A Structure for Efficient Numerical Computation, *Computing in Science and Engineering*, **13**, 22
111. Hunter J. D., 2007. Matplotlib: A 2D Graphics Environment, *Computing in Science & Engineering*, **9**, 90
112. Carnall A. C., 2017. SpectRes: A Fast Spectral Resampling Tool in Python, [p. arXiv:1705.05165 arXiv:1705.05165](https://arxiv.org/abs/1705.05165)

Acknowledgements

We thank Laura Keating, Harley Katz, Callum Witten, William McClymont, Arjen van der Wel, John Chisholm, Danielle Berg, and Masami Ouchi for useful discussions. This work is based on observations made with the National Aeronautics and Space Administration (NASA)/European Space Agency (ESA)/Canadian Space Agency (CSA) JWST. The data were obtained from the Mikulski Archive for Space Telescopes at the STScI, which is operated by the Association of Universities for Research in Astronomy, Inc., under NASA contract NAS 5-03127 for JWST. These observations are associated with programmes 1180, 1210, 1286, 1287, and 3215. JW, RM, WMB, FDE, and JS acknowledge support from the Science and Technology Facilities Council (STFC), by the European Research Council (ERC) through Advanced Grant 695671 “QUEENCH”, by the UK Research and Innovation (UKRI) Frontier Research grant RISEandFALL. JW also gratefully acknowledges support from the Cosmic Dawn Center through the DAWN Fellowship. The Cosmic Dawn Center (DAWN) is funded by the Danish National Research Foundation under grant No. 140. BDJ, BER, FS, PAC, DJE, CNAW, and YZ acknowledge support from the JWST/NIRCam contract to the University of Arizona, NAS5-02015. BER also acknowledges support from JWST Program 3215. ST acknowledges support by the Royal Society Research Grant G125142. AJC, AJB, AS, JC, and GCJ acknowledge funding from the “FirstGalaxies” Advanced Grant from the ERC under the European Union’s Horizon 2020 research and innovation programme (Grant agreement No. 789056). RS acknowledges support from a STFC Ernest Rutherford Fellowship (ST/S004831/1). SAI acknowledges support from the JWST MIRI Science Team Lead, grant 80NSSC18K0555, from NASA Goddard Space Flight Center to the University of Arizona. SAR acknowledges grant PID2021-127718NB-I00 funded by the Spanish Ministry of Science and Innovation/State Agency of Research (MICIN/AEI/10.13039/501100011033). This research is supported in part by the Australian Research Council Centre of Excellence for All Sky Astrophysics in 3 Dimensions (ASTRO 3D), through project number CE170100013. SCA acknowledges support by European Union’s HE ERC Starting Grant No. 101040227 “WINGS”. ECL acknowledges support of an STFC Webb Fellowship (ST/W001438/1). DJE is supported as a Simons Investigator. PGP-G acknowledges support from grant PID2022-139567NB-I00 funded by Spanish Ministerio de Ciencia e Innovación MCIN/AEI/10.13039/501100011033, FEDER, UE. HÜ acknowledges funding by the European Union (ERC APEX, 101164796). Views and opinions expressed are however those of the authors only and do not necessarily reflect those of the European Union or the European Research Council Executive Agency. Neither the European Union nor the granting authority can be held responsible for them. The research of CCW is supported by NOIRLab, which is managed by the Association of Universities for Research in Astronomy (AURA) under a cooperative agreement with the National Science Foundation. This study made use of the Prospero high performance computing facility at Liverpool John Moores University. This version of the article has been accepted for publication, after peer review (when applicable) but is not the Version of Record and does not reflect post-acceptance improvements, or any corrections. The Version of Record is available online at: <https://dx.doi.org/10.1038/s41586-025-08779-5>.

Author information

Affiliations

¹Kavli Institute for Cosmology, University of Cambridge, Madingley Road, Cambridge CB3 0HA, UK

²Cavendish Laboratory, University of Cambridge, 19 JJ Thomson Avenue, Cambridge CB3 0HE, UK

³Cosmic Dawn Center (DAWN), Copenhagen, Denmark

⁴Niels Bohr Institute, University of Copenhagen, Jagtvej 128, DK-2200, Copenhagen, Denmark

⁵Department of Physics and Astronomy, University College London, Gower Street, London WC1E 6BT, UK

⁶Steward Observatory, University of Arizona, 933 N. Cherry Avenue, Tucson AZ 85721, USA

⁷Center for Astrophysics | Harvard & Smithsonian, 60 Garden St., Cambridge MA 02138, USA

⁸Department of Astronomy and Astrophysics University of California, Santa Cruz, 1156 High Street, Santa Cruz CA 95054, USA

⁹Department of Physics, University of Oxford, Denys Wilkinson Building, Keble Road, Oxford OX1 3RH, UK

¹⁰Astrophysics Research Institute, Liverpool John Moores University, 146 Brownlow Hill, Liverpool L3 5RF, UK

¹¹Centro de Astrobiología (CAB), CSIC-INTA, Cra. de Ajalvir Km. 4, 28850- Torrejón de Ardoz, Madrid, Spain

¹²European Space Agency (ESA), European Space Astronomy Centre (ESAC), Camino Bajo del Castillo s/n, 28692 Villanueva de la Cañada, Madrid, Spain

¹³Scuola Normale Superiore, Piazza dei Cavalieri 7, I-56126 Pisa, Italy

¹⁴Sorbonne Université, CNRS, UMR 7095, Institut d’Astrophysique de Paris, 98 bis bd Arago, 75014 Paris, France

¹⁵European Southern Observatory, Karl-Schwarzschild-Strasse 2, 85748 Garching, Germany

¹⁶Centre for Astrophysics Research, Department of Physics, Astronomy and Mathematics, University of Hertfordshire, Hatfield AL10 9AB, UK

¹⁷INAF – Osservatorio Astronomico di Brera, via Brera 28, I-20121 Milano, Italy

¹⁸AURA for European Space Agency, Space Telescope Science Institute, 3700 San Martin Drive. Baltimore, MD 21210, USA

¹⁹Department of Astronomy, University of Wisconsin-Madison, 475 N. Charter St., Madison WI 53706, USA

²⁰Max-Planck-Institut für extraterrestrische Physik, Gießenbachstraße 1, 85748 Garching, Germany

²¹NSF’s National Optical-Infrared Astronomy Research Laboratory, 950 North Cherry Avenue, Tucson AZ 85719, USA

²²NRC Herzberg, 5071 West Saanich Rd, Victoria BC V9E 2E7, Canada

Author contributions

JW and PJ led the analysis and the writing of this paper, with key contributions from AJB, AJC, AS, BDJ, BER, FS, JMH, MC, RM, RS, SCa, and ST. AJB, CW, FDE, GCJ, JC, JW, KB, MC, NK, PJ, RM, SAr, SCa, and SCh contributed to the development and commissioning of the NIRSpec instrument and the reduction and analysis of the NIRSpec data presented. BDJ, BER, CCW, CNAW, DJE, FS, KNH, PAC and ST contributed to the development and commissioning of the NIRCam instrument and the reduction and analysis of the NIRCam data presented. JMH and SAI contributed to the reduction and analysis of the MIRI data presented. AJB, BDJ,

BER, CCW, CNAW, CW, DJE, ECL, FDE, HÜ, JC, JS, KNH, MVM, PPGP, PJ, and RM contributed to the design and execution of the JADES program. AJB, BER, CW, DJE, and ST serve on the JADES Steering Committee. RB, WMB, PR, and YZ provided comments on the manuscript.

Correspondence

Correspondence should be addressed to J. Witstok.

Ethics declarations

Competing interests

The authors declare no competing interests.

Supplementary information

NIRCam imaging

The NIRCam imaging data set in the JOF comprises 14-band imaging of uniform depth, each having 5σ limits below ~ 3 nJy for a point source^{14,16}. A false-colour image centred on JADES-GS-z13-1-LA created from stacked NIRCam image mosaics is shown in Supplementary Material Fig. 1. The blue channel is the mean of the F090W and F115W filters, green similarly combines F150W and F162M, while red is a stack of F182M, F200W, and F210M (panel d of Fig. 1 was created similarly with all available filters). Photometric redshifts of nearby galaxies have been derived with EAZY¹¹³ as outlined in Hainline et al.¹⁵.

NIRSpec data reduction

We considered various reduction variations, including one that reduces self-subtraction in cases where the emission is extended over multiple micro-shutters by only considering the two outer nod positions instead of the default three. We have verified that the differences between this reduction and the default one considering all nod positions are minimal, including for the emission line observed at $\lambda_{\text{obs}} \approx 1.7 \mu\text{m}$. The same is true for reduction variants where one-dimensional spectra are extracted over the central three or five spatial pixels (corresponding to $0.3''$ or $0.5''$ respectively), as expected given the compactness of JADES-GS-z13-1-LA (Methods). We therefore base our analysis on 3-pixel extractions considering all three nodding positions to maximise the SNR. Additional path losses are accounted for through a comparison with NIRCam photometry, as discussed in the Methods.

The pipeline independently produces two- and one-dimensional spectra from all reduced sub-exposures, of which there are a substantial number for JADES-GS-z13-1-LA (48 for the PRISM and 12 for each of the R1000 gratings). Since cosmic ray impacts and noisy pixels are not always fully captured in the ramp fitting⁶¹ and occasionally introduce a sharp excess of flux in these individual sub-exposures, the standard reduction pipeline adopts iterative sigma clipping⁵⁶ for each wavelength bin before co-adding the reduced one-dimensional spectra. This combination process weights individual sub-spectra inversely by the pipeline error estimate squared. The combination of two-dimensional spectra is performed separately⁵⁶, and therefore the final combined two-dimensional spectrum (as shown in Fig. 1) is not used to directly extract one-dimensional spectra. Recently, however, several refinements to this standard procedure were presented in a detailed investigation⁹ (see also ref.¹¹⁴) of ultra-deep NIRSpec/PRISM measurements of two $z > 10$ galaxies benefiting from a large number of sub-exposures (186 and 138 respectively), which we follow here to obtain our fiducial ('sigma-clipped') spectrum.

Specifically, Hainline et al.⁹ introduced two additional masking steps aimed at removing obviously spurious flux values at the beginning of the combination process. In each step, the median flux value and median pipeline error estimate for each wavelength bin are calculated across available sub-exposures. Wavelength bins of sub-spectra where flux values deviate by more than five times the median error from the median flux, or where the pipeline error estimate exceeds five times its median, were eliminated. Subsequently, five iterations of sigma clipping removed flux values deviating from the average of the surviving entries in the bin by more than three times the sample standard deviation. Finally, the individual sub-spectra were co-added simply by averaging the surviving entries in each wavelength bin. As in Hainline et al.⁹ and Curti et al.¹¹⁴, we constructed 2000 bootstrapped realisations of the final combined spectrum from which we

derived a covariance matrix. Crucially, this covariance matrix directly captures all possible sources of statistical fluctuations present in the data (including those not explicitly taken into account by the default pipeline) as well as the significant degree of correlation in the noise of adjacent wavelength bins.

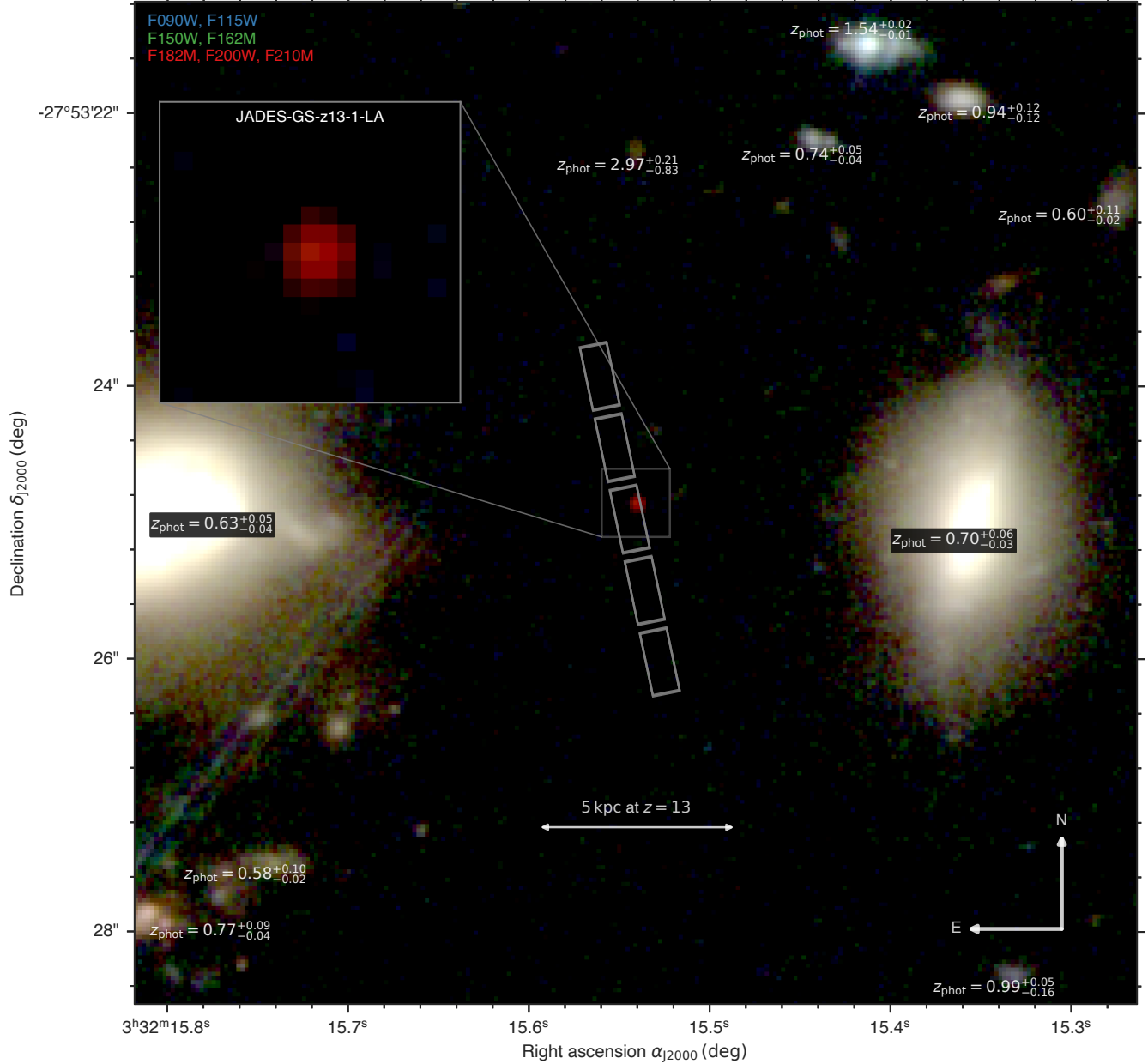
We note that while the intra-shutter location of JADES-GS-z13-1-LA is nearly identical across the two visits (Fig. 1), the sub-exposures follow a three-point nodding pattern, and the employed micro-shutters differ by one column between the two visits (quadrant 3, row 237, column 87 versus quadrant 3, row 237, column 86). As a result, the two-dimensional spectra, including the emission line at $\lambda_{\text{obs}} \approx 1.7 \mu\text{m}$, are shifted vertically by ~ 15 pixels on the detector over the range of the 48 sub-exposures, thus minimising the potential impact of bad pixels. We have performed careful visual inspection of the raw NIRSpec exposure frames to verify the spectrum does not suffer from overlapping targets or contamination from other (failed) open micro-shutters. Finally, there are no signs of hot pixels or significant particle hits affecting the line at $\lambda_{\text{obs}} \approx 1.7 \mu\text{m}$ in the extracted spectrum: in the four wavelength bins where the line appears in the combined PRISM spectrum, the refined sigma-clipping algorithm described above has classified 46 out of 48 values as valid for one bin, while all 48 values in the remaining three bins were deemed valid.

NIRSpec/PRISM spectra

In Supplementary Material Fig. 2, we compare different one-dimensional PRISM spectra of JADES-GS-z13-1-LA, including our fiducial spectrum, obtained from the refined sigma-clipping procedure applied on 3-pixel extractions of all available sub-exposures (NIRSpec data reduction), and the default STScI pipeline spectrum. From this comparison, we conclude these generally agree very well, although a number of noise spikes can be seen in the STScI spectrum. We also show spectra obtained separately from the two visits, which both show good agreement with the combined spectrum, including for the emission line observed at $\lambda_{\text{obs}} \approx 1.7 \mu\text{m}$.

Furthermore, we provide a comparison with the NIRSpec/PRISM spectrum of GS-9422 at $z = 5.94$ (JADES-GS+53.12175-27.79763 in Bunker et al.⁵⁶; see also refs.^{44, 74, 115}), whose spectrum simultaneously displays strong Ly α emission, a Balmer jump, and a steep turnover seen in the UV (rest-frame wavelengths below $\lambda_{\text{emit}} \lesssim 1500 \text{ \AA}$). To guide the eye, Supplementary Material Fig. 2 shows the 2γ continuum for gas at electron density of $n_e = 10^3 \text{ cm}^{-3}$ and electron temperature of $T_e = 20\,000 \text{ K}$ (though we note that unlike the normalisation, the shape of the 2γ continuum does not depend on these conditions⁷⁵), which, like the spectrum of GS-9422, is shifted in wavelength to $z = 13$ and rescaled to match the observed flux density of JADES-GS-z13-1-LA at $\lambda_{\text{emit}} = 1500 \text{ \AA}$.

A detailed view of the PRISM wavelength bins near the emission line observed at $\lambda_{\text{obs}} \approx 1.7 \mu\text{m}$ is shown in Supplementary Material Fig. 3. We performed jackknife resampling of all sub-spectra to independently estimate the uncertainty on the mean flux measured in each wavelength bin across all sub-exposures (in the absence of any masking). These are in excellent agreement the fiducial, sigma-clipped spectrum and uncertainty from the bootstrapped covariance matrix (NIRSpec data reduction), suggesting the measurements are regularly distributed without extreme outliers. We also computed the (unmasked) integrated flux across four bins with $\text{SNR} > 1$ for each sub-spectrum separately. The resulting $\text{SNR} = 6.4$ on the integrated flux estimated using jackknife resampling again agrees well with the SNR estimated via the sigma-clipped spectrum and corresponding bootstrapped covariance matrix, as will be discussed in Emission

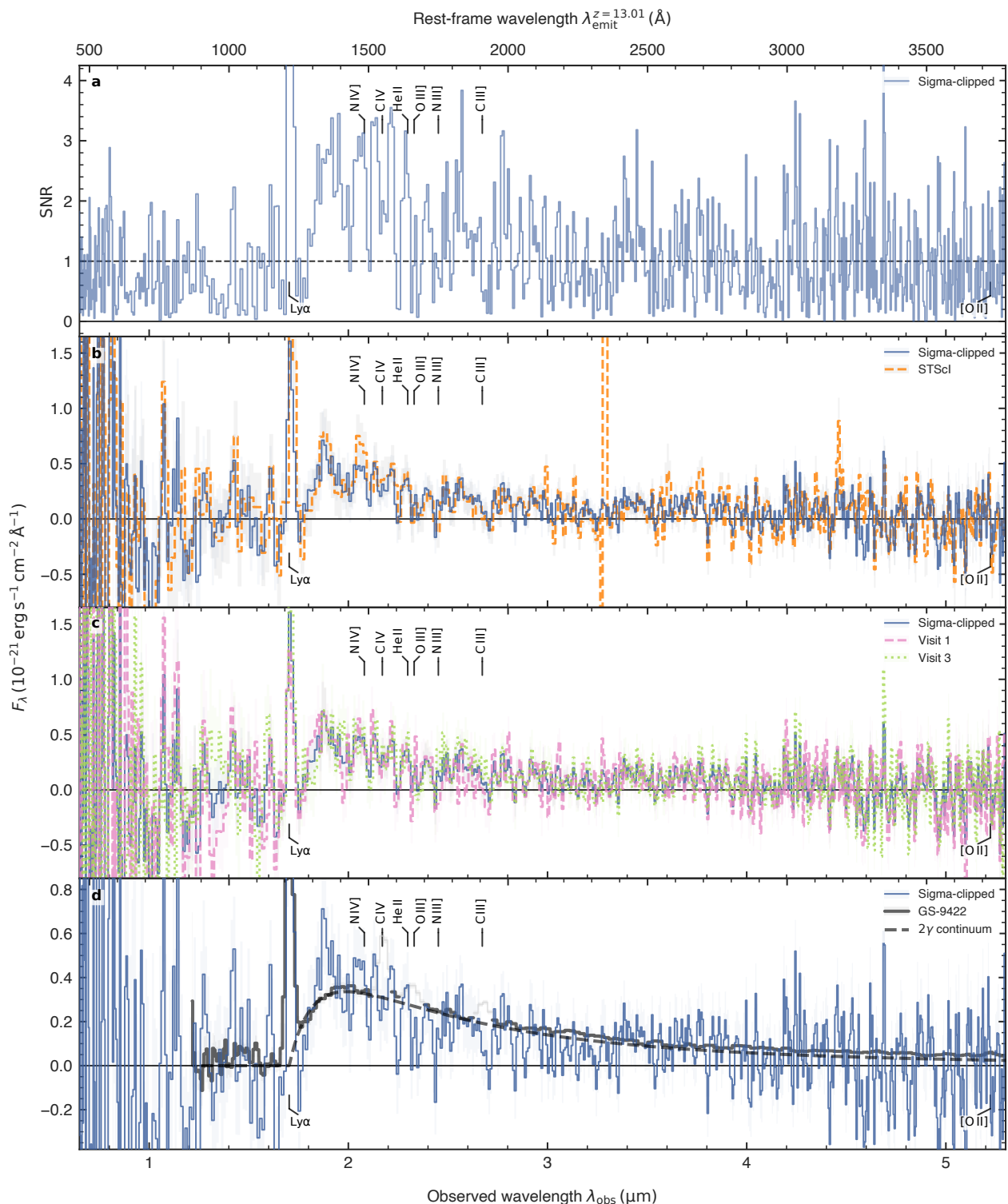


Supplementary Material Fig. 1 | NIRCam false-colour image of JADES-GS-z13-1-LA and its surroundings. The image shows stacks of the F090W and F115W filters as the blue channel, the F150W and F162M filters as green, and F182M, F200W, and F210M as red. To the bottom left, a diffraction spike can be seen stretching diagonally across the image, coming from a star located just outside the field of view. Annotations show the photometric redshifts of nearby sources, including two extended low-redshift galaxies. The placement of the NIRSpec micro-shutters is shown in grey. At the bottom centre, a scale of 5 kpc at $z = 13.0$ is indicated.

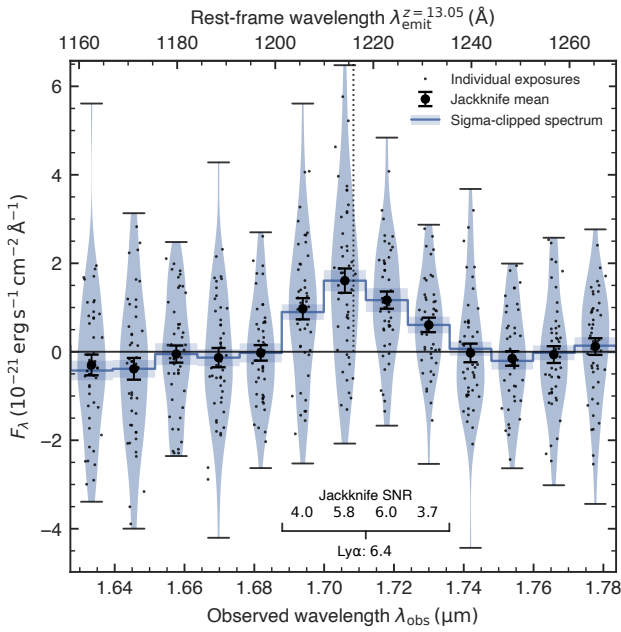
line properties. The STScI reduction, on the other hand, nominally returns a higher significance for the line detection ($\text{SNR} = 8.5$), likely reflecting a slight underestimation of the (correlated) noise (NIRSpec data reduction).

We consider here whether the emission line at $1.71\text{ }\mu\text{m}$ may be due to contamination of the micro-shutter by a foreground source that is aligned with JADES-GS-z13-1-LA by chance and remains undetected in the continuum. Firstly, such a low-redshift interloper must have an exceptionally high EW to respect the stringent non-detections in the bluest NIRCam filters (e.g. the F150W 3σ constraint implies

an observed $\text{EW} \gtrsim 10\,000\text{ }\text{\AA}$ if the continuum were flat in F_V). Therefore, the line could realistically only be $\text{H}\alpha$ at $z \approx 1.60$, where $\text{Pa}\alpha$ from the same foreground source would be observed at $4.88\text{ }\mu\text{m}$, or $[\text{O III}]\lambda 5008\text{ }\text{\AA}$ at $z \approx 2.41$ where the $\text{H}\alpha$ and $[\text{N II}]$ complex would fall at $2.24\text{ }\mu\text{m}$. The absence of any accompanying line detections in the first case implies $\text{H}\alpha/\text{Pa}\alpha > 13.8$ (2σ), in tension with the case-B ratio⁹¹ of $\text{H}\alpha/\text{Pa}\alpha \approx 10$ which can only be decreased by dust attenuation. Alternatively, for the interloper to be at $z \approx 2.41$ requires a line ratio $([\text{O III}] / (\text{H}\alpha + [\text{N II}]) > 7.7$ at 2σ) completely incompatible with observed properties of $z \sim 2$ galaxies¹¹⁶. Leaving



Supplementary Material Fig. 2 | Comparison of NIRSpec/PRISM spectra of JADES-GS-z13-1-LA. **a**, SNR on individual wavelength bins for the sigma-clipped spectrum combining all sub-exposures (also displayed in other panels). The uncertainty on individual spectral bins considered here only represents diagonal elements of the covariance matrix. **b**, Comparison with the default STScI pipeline reduction (see NIRSpec observations and data reduction for details). **c**, Comparison with spectra of the two visits separately. **d**, Comparison of the spectrum of JADES-GS-z13-1-LA with that of GS-9422 (strong UV lines greyed out to ease comparison) and the two-photon (2γ) continuum (both rescaled; see text for details). Shading in panels b through d shows 1σ uncertainty. All panels show the expected locations of key UV emission lines: Ly α (detected), N IV, C IV, He II, O III, N III, C III, and [O II] (all undetected).



Supplementary Material Fig. 3 | Individual sub-spectra of JADES-GS-z13-1-LA around 1.7 μm. Our fiducial, sigma-clipped spectrum is shown by the step-wise blue line, with shading representing the 1σ uncertainty for each individual spectral bin as retrieved from the diagonal element of the covariance matrix. The flux values extracted from individual sub-exposures are shown as small black circles within each wavelength bin (slightly offset in the wavelength direction for visualisation). Their distribution is illustrated with a kernel-density estimate shown by a blue swath, enclosed by short horizontal black bars indicating the flux extrema. Larger black circles represent their mean, with errorbars showing the 68% confidence interval estimated via jackknife resampling. The jackknife SNR is annotated for four individual bins with $\text{SNR} > 1$, as well as for the combined flux across these four bins.

aside EW arguments, for the line to be the $[\text{O II}]\lambda 3727, 3730\text{ Å}$ doublet ($[\text{O II}]$) at $z \approx 3.58$, similarly unprecedented line ratios would be required ($[\text{O II}]/\text{H}\beta > 8.4$ and $[\text{O III}]/[\text{O II}] < 0.11$ at 2σ).

We conclude the only consistent explanation is that the line is Ly α at $z \approx 13$. However, we note its observed properties also cannot be due to the extended Ly α photon-diffusion emission predicted to surround galaxies before reionisation: it has been shown this should extend over a physical size of $\approx 1\text{ pMpc}$ ²⁷ and as a result, the diffuse Ly α emission has extremely low surface brightness¹¹⁷, orders of magnitude lower than observed in the spectrum of JADES-GS-z13-1-LA taken over a solid angle of $0.199'' \times 0.461''$ spanned by a micro-shutter on sky¹⁷. Moreover, our nodding background subtraction technique would largely self-subtract this signal that is predicted to have approximately uniform central surface brightness²⁷.

Synthetic photometry and path-loss corrections

To assess the quality of the NIRSpec spectrophotometry and quantify any additional path losses not already accounted for by the data reduction pipeline (see NIRSpec observations and data reduction), we created ‘synthetic’ NIRSpec photometry to directly compare against the available NIRCam measurements (cf. Extended Data Table 1). Noting all variations of the NIRSpec data reduction yield consistent results, including between the 5-pixel and 3-pixel extractions (Supplementary information), we calculated synthetic flux densities by

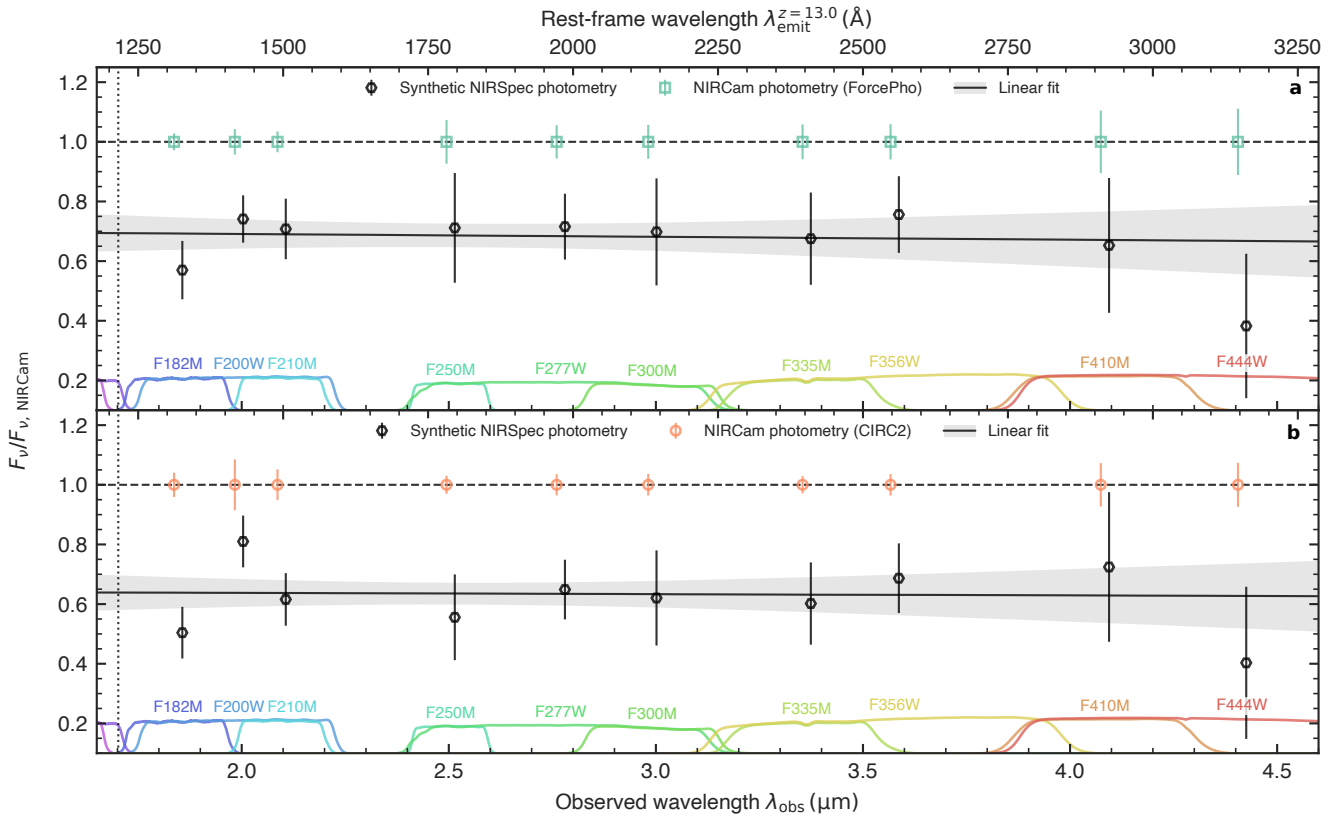
convolving the sigma-clipped spectrum (with only the default point-source path-loss correction applied; see NIRSpec observations and data reduction) with the NIRCam filter profiles. The corresponding uncertainties were derived using the full covariance matrix and therefore take into account correlated noise properties directly estimated from the measurements. A comparison between the different photometry variants considered here, as derived from NIRSpec (synthetic) and NIRCam (FORCEPHO and CIRC2; see Photometric measurements), is provided in Supplementary Material Fig. 4.

We used the EMCEE¹⁰⁷ package to perform a linear fit to the ratios of the synthetic NIRSpec photometry to the NIRCam photometry (both the FORCEPHO and CIRC2 measurements) as a function of wavelength. Between FORCEPHO and CIRC2, we consistently find the NIRSpec fluxes are approximately $0.7\times$ those measured by NIRCam (a difference of about 0.4 mag). There is no clear dependence on the observed wavelength: in the FORCEPHO case, the linear fit has a slope of $-0.01 \pm 0.06\text{ μm}^{-1}$, and the CIRC2 photometry has $0.00 \pm 0.05\text{ μm}^{-1}$. We note that the point-source approximation used by the pipeline to apply the initial path-loss corrections (NIRSpec observations and data reduction) should be valid in the case of JADES-GS-z13-1-LA, as it is essentially unresolved by NIRCam (see Photometric measurements). However, these corrections are subject to a systematic uncertainty on the intra-shutter position introduced by the limited pointing accuracy of the MSA, which is anticipated¹⁷ to be of the order of 25 mas (i.e. comparable to or larger than the size of JADES-GS-z13-1-LA). This effect is enhanced for sources close to the micro-shutter edge (as is the case for JADES-GS-z13-1-LA; Fig. 1), where the path-loss correction shows the largest gradient⁶¹.

UV magnitude and slope

We first measured the absolute UV magnitude M_{UV} and slope β_{UV} directly from the different sets of photometry. To perform an unbiased inference of these parameters, we consider filters redwards of $\lambda_{\text{obs}} = 2.0\text{ μm}$ (i.e. from F210M on), corresponding to rest-frame wavelengths $\lambda_{\text{emit}} \gtrsim 1500\text{ Å}$ at $z = 13$, thus avoiding the strong spectral break and line (Fig. 1). The results are tabulated Extended Data Table 1. Given the uncertainty of the systemic redshift (as discussed in the Spectral modelling section of the Methods), reported uncertainties on the UV magnitude conservatively take into account a systematic uncertainty of $\Delta z = 0.05$. The UV slope is reported for fits taking into account all available NIRCam filters, covering the rest frame at $\lambda_{\text{emit}} \lesssim 3500\text{ Å}$. Alternatively, since empirical measurements of UV slopes in the literature use slightly different wavelength ranges (e.g. refs.^{31, 118–121}), we also report the UV slope only using NIRCam filters below $\lambda_{\text{obs}} \approx 3.5\text{ μm}$ (i.e. up to and including F335M), corresponding to $\lambda_{\text{emit}} \lesssim 2500\text{ Å}$. This reflects the commonly adopted prescription by Calzetti et al.¹²² and more closely mimics the fitting range discussed in Spectral modelling.

The UV magnitude inferred from the (uncorrected) NIRSpec measurements is 0.4–0.5 mag fainter than those from NIRCam, reflecting the discrepancy found in Synthetic photometry and path-loss corrections. Based on the CIRC2 photometry, we find a UV magnitude of $M_{\text{UV}} = -18.66^{+0.04}_{-0.04}$, in good agreement with $M_{\text{UV}} = -18.73 \pm 0.04$ reported by Robertson et al.¹⁶ (corrected for differences in the adopted cosmology) based on Kron¹²³ photometry. Among the three sets of photometry considered here, our best-fitting UV slopes are consistently very steep ($\beta_{\text{UV}} \lesssim -2.7$), again agreeing with $\beta_{\text{UV}} = -2.73 \pm 0.13$ found by Robertson et al.¹⁶ when considering the full wavelength range observed by NIRCam ($\lambda_{\text{emit}} \lesssim 3500\text{ Å}$). We find a considerably steeper slope yet ($\beta_{\text{UV}} < -3$) in the wavelength



Supplementary Material Fig. 4 | Comparison between NIRCam and NIRSpec (spectro)photometry of JADES-GS-z13-1-LA. Synthetic NIRSpec photometry (see Synthetic photometry and path-loss corrections) is plotted relative to the FORCEPHO (panel a) and CIRC2 (panel b) photometry in each available NIRCam filter redwards of the observed wavelength of Ly α at $z = 13$ (dotted vertical line).

range up to $\lambda_{\text{emit}} \lesssim 2500 \text{ \AA}$ (though with larger uncertainties, as a result of the smaller wavelength range and number of data points). Finally, we provide an estimate of the bolometric luminosity (L_{bol}) by integrating the power law with a lower bound at $\lambda_{\text{He II}} = 227.84 \text{ \AA}$ (i.e. the He II ionisation edge at 54.4 eV, where stellar SEDs are typically suppressed³²).

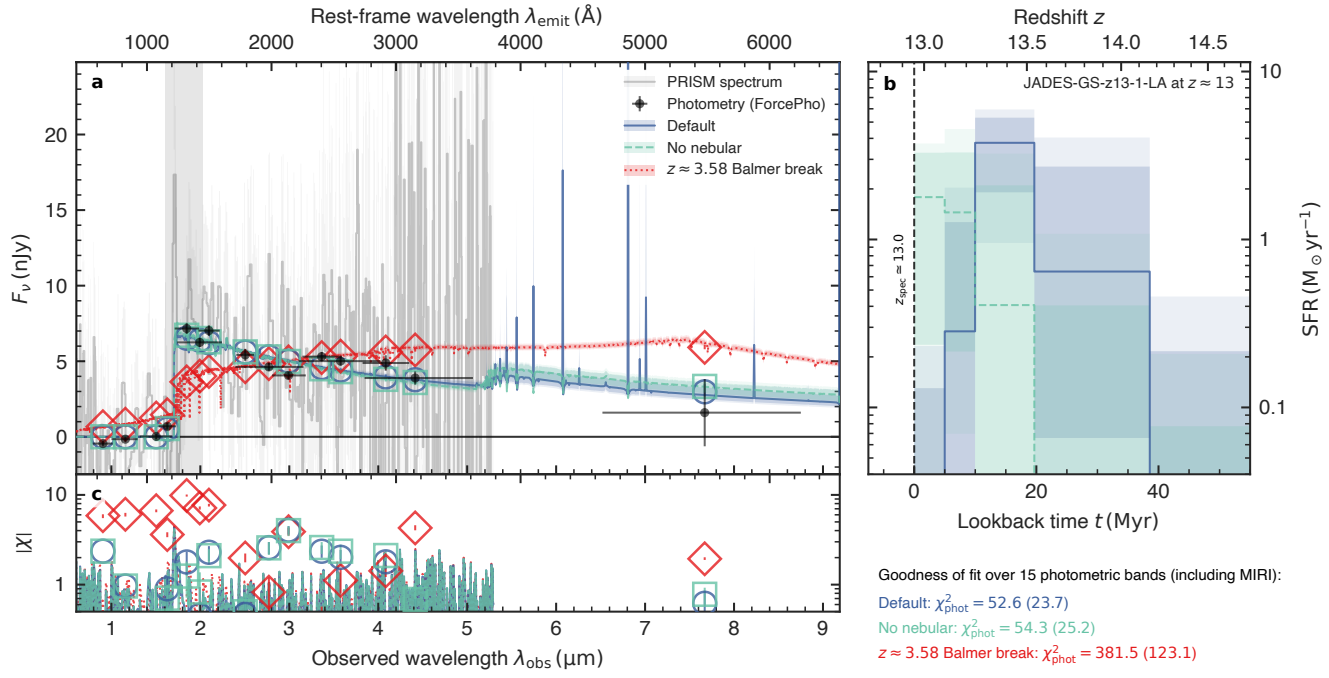
Stellar population synthesis modelling

We modelled the full SED of JADES-GS-z13-1-LA taking into account NIRCam photometry* as well as the NIRSpec/PRISM measurements (the 3-pixel extraction from the default pipeline) with standard SPS models. Specifically, we follow the procedure outlined in Witstok et al.¹¹, using the Bayesian Analysis of Galaxies for Physical Inference and Parameter ESTimation (BAGPIPES¹⁰⁴) set up with v2.2.1 Binary Population and Spectral Synthesis (BPASS¹²⁴) binary-star models, assuming the default BPASS IMF (stellar mass upper limit of $300 M_{\odot}$). We masked the NIRSpec measurements in the spectral region around Ly α , $1150 \text{ \AA} < \lambda_{\text{emit}} < 1450 \text{ \AA}$, where the complex spectral shape featuring a strong Ly α emission line near a steep turnover cannot be reproduced straightforwardly by standard SED

modelling codes such as BAGPIPES, and therefore will be modelled separately in Spectral modelling.

We adopted the non-parametric star formation history (SFH) of Leja et al.¹²⁵ with 6 bins in lookback time t . As in Tacchella et al.¹²⁶, the first two of these are spaced between $0 \text{ Myr} < t < 5 \text{ Myr}$ and $5 \text{ Myr} < t < 10 \text{ Myr}$, with logarithmic spacing for the 4 remaining bins up to $z = 20$. We adopted the ‘bursty-continuity’ prior for the SFR ratio between adjacent time bins¹²⁷, having confirmed that consistent results are achieved for a more smoothly varying SFH (‘standard continuity’). We varied the total stellar mass formed over $0 < M_* < 10^{15} M_{\odot}$ and stellar metallicity across $0.001 Z_{\odot} < Z_* < 1.5 Z_{\odot}$, both with log-uniform priors. Our default model includes nebular emission, which BAGPIPES derives from CLOUDY models¹⁰⁶, where the nebular metallicity is fixed to the stellar one. The incident radiation field is set by the relevant SPS models, modulated by a freely varying ionisation parameter ($-3 < \log_{10} U < -0.5$). We included a flexible Charlot & Fall¹²⁸ prescription to model the dust attenuation, as detailed in Witstok et al.¹¹ (see also ref. 129). The PRISM spectrum was assumed to have a spectral resolution as derived for a uniformly illuminated micro-shutter, noting that fitting only to the continuum (while masking the observed line and break) the precise spectral resolution will not significantly impact the modelled observed spectrum. A first-order polynomial correction to the spectroscopic data¹³⁰ was included to account for the mild discrepancy between NIRSpec and NIRCam (Synthetic photometry and path-loss corrections).

* We have verified that including the MIRI/F770W photometric measurement does not noticeably change our findings, so we chose not to include it in the fitting results shown here unless explicitly mentioned.



Supplementary Material Fig. 5 | SED modelling of JADES-GS-z13-1-LA. Three different SPS models produced by BAGPIPES are shown: the default setup (circles), a model without nebular emission ('No nebular', squares), and a forced low-redshift model ($z \approx 3.58$ Balmer break, diamonds; see Stellar population synthesis modelling for details). **a**, Observed NIRCam (FORCEPHO) and MIRI photometry (black points) and NIRSpec/PRISM spectrum (grey line; smoothed by a 3-pixel median filter for visualisation), overlaid by the three models (lines according to the legend in the top right and open symbols). Error bars on the photometry and light-grey shading around the spectrum represent 1σ uncertainties; darker (lighter) shading around the model lines shows 1σ (2σ) variation in the posterior distribution. **b**, Residuals between the observations and modelled spectra and photometry expressed in terms of the absolute value of χ , the difference normalised by 1σ observational uncertainty. Goodness-of-fit statistics in the form of χ^2 calculated over the 15 photometric bands (including the MIRI/F770W measurement) are annotated (conservative estimates in brackets). **c**, Inferred SFH in the two $z \approx 13$ models (default and without nebular emission; shading as in panel a).

In our default model, we allow the redshift to vary within an interval of $\Delta z = 0.1$ centred on $z = 13.0$, so that we may explicitly marginalise over the uncertainty of the systemic redshift (further discussed in Spectral modelling). In addition, we considered a variation of the default model where we explicitly turn off nebular emission: this would be the case if the galaxy has a LyC escape fraction close to $f_{\text{esc, LyC}} = 100\%$. The resulting best-fitting models are shown in Supplementary Material Fig. 5 and summarised in Supplementary Material Table 1.

Also shown in Supplementary Material Fig. 5 is an alternative ('Balmer-break') model forced to be at lower redshift by centring the $\Delta z = 0.1$ interval on $z = 3.583$ instead, in which case the observed spectral break would correspond to a Balmer break and the (in this case not masked) observed emission line would be [O II] (see Emission-line properties). When fitting this model, we include the MIRI/F770W photometric point. In agreement with Hainline et al.¹⁵ and Robertson et al.¹⁶, we find this low-redshift solution produces a poor fit to the observed SED of JADES-GS-z13-1-LA ($\chi^2 = 381.5$ over 15 NIRCam and MIRI bands), whereas the data are reproduced much better by a model galaxy at $z \approx 13.0$ instead ($\chi^2 = 52.6$ in the default model).

Even so, the comparatively high χ^2 (with $p = 4.5 \times 10^{-6}$ for the default model) indicates that photometric errors are potentially underestimated, or that the standard SPS models fall short of accurately describing the data. While the FORCEPHO photometry circumvents the correlated noise between pixels in the mosaic images, it may still

suffer from a degree of systematic uncertainty, including from any imperfections in the sky background subtraction. This effect is taken into account empirically by the aperture photometry (CIRC2), where the estimated uncertainty considers the scatter found in a number of randomly placed empty apertures, a detailed discussion of which can be found in Rieke et al.⁵⁵. The true statistical errors therefore likely consist of a combination of the nominal uncertainty estimated as part of the FORCEPHO modelling and CIRC2 aperture photometry (which covers approximately 70% of the encircled energy of the F444W PSF). When we conservatively combine the estimated FORCEPHO and CIRC2 photometric uncertainties (treating them as statistically independent) to better account for systematic effects, we instead find a more reasonable $\chi^2 = 23.7$ ($p = 0.070$).

Interestingly, we find the goodness of fit in the absence of nebular emission ($\chi^2 = 54.3$ or more conservatively $\chi^2 = 25.2$) to be essentially the same as in the default model, even if the inferred SFHs vary substantially between these models: the SFH in the model without nebular emission steadily increases, whereas the default model prefers an SFH that rises initially, but subsequently declines over the last 10 Myr. We conclude this downturn in SFH must be artificial, and only preferred by the default model in order to reproduce the very steep UV slope of $\beta_{\text{UV}} \lesssim -2.7$ independently measured both by NIRCam and NIRSpec (see UV magnitude and slope), as this requires reducing the number of very young (< 10 Myr) OB-type stars, which produce a large number of ionising photons at fixed UV luminosity³², thus minimising the contribution of nebular-continuum

Supplementary Material Table 1 | Stellar properties of JADES-GS-z13-1-LA.

Quantity	BAGPIPES		BEAGLE
	Default	No nebular	$f_{\text{esc, LyC}} \neq 0$
M_* ($10^7 M_\odot$)	$5.5^{+2.1}_{-1.2}$	$2.7^{+1.8}_{-0.7}$	$2.6^{+3.5}_{-1.5}$
Σ_* ($10^3 M_\odot \text{ pc}^{-2}$)	$> 7.1^{+2.8}_{-1.6}$	$> 3.5^{+2.3}_{-0.9}$	$> 3.3^{+4.6}_{-2.0}$
Z_* (Z_\odot)	$0.3^{+0.8}_{-0.1} \%$	$0.6^{+1.1}_{-0.3} \%$	$2^{+10}_{-1} \%$
SFR_{10} ($M_\odot \text{ yr}^{-1}$)	$0.19^{+0.51}_{-0.17}$	$1.84^{+0.55}_{-0.62}$	$0.67^{+0.36}_{-0.18}$
Σ_{SFR} ($M_\odot \text{ yr}^{-1} \text{ kpc}^{-2}$)	$> 25^{+66}_{-21}$	$> 240^{+71}_{-81}$	$> 87^{+47}_{-23}$
t_* (Myr)	22^{+9}_{-6}	11^{+13}_{-6}	21^{+38}_{-15}
A_V (mag)	$0.04^{+0.04}_{-0.03}$	$0.11^{+0.08}_{-0.07}$	$0.08^{+0.19}_{-0.05}$
$\log_{10} U$	$-1.91^{+0.82}_{-0.79}$	—	$-2.59^{+0.91}_{-0.86}$
$f_{\text{esc, LyC}}$	0*	1*	$0.81^{+0.14}_{-0.32}$

Best-fitting parameters, taken as the median of their marginalised posterior, are shown for the BAGPIPES and BEAGLE models with different assumptions on nebular emission (see Stellar population synthesis modelling). Error bars represent a 1σ uncertainty (16th and 84th percentiles). Rows: stellar mass (M_*) in 10^7 Solar masses, stellar mass surface density (Σ_*) in 10^3 Solar masses per square parsec, stellar metallicity (Z_*) in units of Solar metallicity, star formation rate in Solar masses per year averaged on a timescale of 10 Myr (SFR_{10}), its corresponding surface density (Σ_{SFR}) in Solar masses per year per square kiloparsec, mass-weighted stellar age (t_*) in Myr, visual dust extinction (A_V) in magnitudes, ionisation parameter U (if applicable), and ionising-photon escape fraction ($f_{\text{esc, LyC}}$).

* Value is fixed in this model.

emission (which typically has $\beta_{\text{UV}} \approx -2$; refs. 29, 131) that drives the UV slope upwards^{119–121,132}.

The tendency towards a high LyC escape fraction is independently confirmed by BEAGLE (Bayesian Analysis of GaLaxy sEds¹⁰⁵) modelling with varying $f_{\text{esc, LyC}}$, largely as described in Curtis-Lake et al.³. Briefly, we fitted the NIRSpec/PRISM spectrum only, again masking the spectral region around Ly α , $1150 \text{ \AA} < \lambda_{\text{emit}} < 1450 \text{ \AA}$. We assumed a constant SFH and a Chabrier¹³³ IMF with stellar mass upper limit of $300 M_\odot$. Reassuringly, the best-fitting parameters (Supplementary Material Table 1) are in good agreement with the BAGPIPES results despite different approaches, particularly considering the absence of normalisation to the NIRCam photometry in the BEAGLE fit. The BEAGLE fit yields a posterior $f_{\text{esc, LyC}} = 0.81^{+0.14}_{-0.32}$ (median and 16th-84th percentiles).

References (continued)

113. Brammer G. B., van Dokkum P. G., Coppi P., 2008. EAZY: A Fast, Public Photometric Redshift Code, *ApJ*, **686**, 1503
114. Curti M., et al., 2024. JADES: The star-formation and chemical enrichment history of a luminous galaxy at $z \sim 9.43$ probed by ultra-deep JWST/NIRSpec spectroscopy, p. arXiv:2407.02575 arXiv:2407.02575
115. Li Y., Leja J., Johnson B. D., Tacchella S., Naidu R. P., 2024. No Top-heavy Stellar Initial Mass Function Needed: The Ionizing Radiation of GS9422 Can Be Powered by a Mixture of an Active Galactic Nucleus and Stars, *ApJ*, **969**, L5
116. Shapley A. E., et al., 2015. The MOSDEF Survey: Excitation Properties of $z \sim 2.3$ Star-forming Galaxies, *ApJ*, **801**, 88
117. Padmanabhan H., Loeb A., 2024. Intergalactic Lyman- α haloes before reionization are detectable with JWST, *J. Cosmology Astropart. Phys.*, **2024**, 059
118. Cullen F., et al., 2023. The ultraviolet continuum slopes (β) of galaxies at $z \simeq 8–16$ from JWST and ground-based near-infrared imaging, *MNRAS*, **520**, 14
119. Topping M. W., et al., 2024. The UV continuum slopes of early star-forming galaxies in JADES, *MNRAS*, **529**, 4087
120. Cullen F., et al., 2024. The ultraviolet continuum slopes of high-redshift galaxies: evidence for the emergence of dust-free stellar populations at $z > 10$, *MNRAS*, **531**, 997
121. Austin D., et al., 2024. EPOCHS III: Unbiased UV continuum slopes at $6.5 < z < 13$ from combined PEARLS GTO and public JWST NIRCam imaging, p. arXiv:2404.10751 arXiv:2404.10751
122. Calzetti D., Kinney A. L., Storchi-Bergmann T., 1994. Dust Extinction of the Stellar Continua in Starburst Galaxies: The Ultraviolet and Optical Extinction Law, *ApJ*, **429**, 582
123. Kron R. G., 1980. Photometry of a complete sample of faint galaxies., *ApJS*, **43**, 305
124. Eldridge J. J., et al., 2017. Binary Population and Spectral Synthesis Version 2.1: Construction, Observational Verification, and New Results, *Publ. Astron. Soc. Australia*, **34**, e058
125. Leja J., Carnall A. C., Johnson B. D., Conroy C., Speagle J. S., 2019. How to Measure Galaxy Star Formation Histories. II. Nonparametric Models, *ApJ*, **876**, 3
126. Tacchella S., et al., 2023. JWST NIRCam + NIRSpec: interstellar medium and stellar populations of young galaxies with rising star formation and evolving gas reservoirs, *MNRAS*, **522**, 6236
127. Tacchella S., et al., 2022. On the Stellar Populations of Galaxies at $z = 9–11$: The Growth of Metals and Stellar Mass at Early Times, *ApJ*, **927**, 170
128. Charlot S., Fall S. M., 2000. A Simple Model for the Absorption of Starlight by Dust in Galaxies, *ApJ*, **539**, 718
129. Chevallard J., et al., 2019. Simulating and interpreting deep observations in the Hubble Ultra Deep Field with the JWST/NIRSpec low-resolution ‘prism’, *MNRAS*, **483**, 2621
130. Carnall A. C., et al., 2019. The VANDELS survey: the star-formation histories of massive quiescent galaxies at $1.0 < z < 1.3$, *MNRAS*, **490**, 417
131. Saxena A., et al., 2024. Hitting the slopes: A spectroscopic view of UV continuum slopes of galaxies reveals a reddening at $z > 9.5$, p. arXiv:2411.14532 arXiv:2411.14532
132. Byler N., Dalcanton J. J., Conroy C., Johnson B. D., 2017. Nebular Continuum and Line Emission in Stellar Population Synthesis Models, *ApJ*, **840**, 44
133. Chabrier G., 2003. Galactic Stellar and Substellar Initial Mass Function, *PASP*, **115**, 763